

## THE CANADA-FRANCE DEEP FIELDS III: PHOTOMETRIC REDSHIFT DISTRIBUTION TO $I_{\text{AB}} \sim 24$

M. BRODWIN<sup>1</sup>

Department of Astronomy & Astrophysics, University of Toronto, ON M5S 3H8, Canada

S. J. LILLY<sup>1,2</sup> AND C. PORCIANI

Department of Physics, Swiss Federal Institute of Technology (ETH-Zürich), ETH Höenggerberg, CH-8093, Zürich, Switzerland.

H. J. MCCRACKEN

University of Bologna, Department of Astronomy, via Ranzani 1, 40127 Bologna, Italy and  
 Osservatorio Astronomico di Bologna, Bologna, Italy

O. LE FÈVRE<sup>1</sup> AND S. FOUCAUD

Laboratoire d'Astrophysique de Marseille, Traverse du Siphon, 13376 Marseille Cedex 12, France

D. CRAMPTON

Herzberg Institute of Astrophysics, West Saanich Road, Victoria, BC V9E 2E7, Canada

Y. MELLIER

Institut d Astrophysique de Paris, 98 bis Boulevard Arago, 75014 Paris, France and  
 Observatoire de Paris, LERMA, 61 Avenue de l'Observatoire, 75014 Paris, France

*Draft version May 22, 2019*

### ABSTRACT

We compute accurate redshift distributions to  $I_{\text{AB}} = 24$  and  $R_{\text{AB}} = 24.5$  using photometric redshifts estimated from 6-band photometry in the Canada-France Deep Fields-Photometric Redshift Survey (CFDF-PRS). Our photometric redshift algorithm is calibrated using hundreds of CFRS spectroscopic redshifts in the same fields. The dispersion in redshift is  $\sigma/(1+z) \lesssim 0.04$  to the CFRS depth of  $I_{\text{AB}} = 22.5$ , rising to  $\sigma/(1+z) \lesssim 0.06$  at our nominal magnitude and redshift limits of  $I_{\text{AB}} = 24$  and  $z \leq 1.3$ , respectively. We describe a new method to compute  $N(z)$  that incorporates the full redshift likelihood functions in a Bayesian iterative analysis and we demonstrate in extensive Monte Carlo simulations that it is superior to distributions calculated using simple maximum likelihood redshifts. A direct application of our results is in weak lensing cosmic shear studies, in which accurate source and lens plane redshift distributions are required to extract cosmological parameters from the convergence power spectrum. We therefore provide our measured  $I_{\text{AB}}$  and  $R_{\text{AB}}$  redshift distributions, the run of median redshifts, and parametrized fits of our results in various magnitude ranges. We account for both random and systematic errors in our analysis, and discuss the effects of cosmic variance on our survey and on measurements of  $N(z)$  in general.

*Subject headings:* Galaxies: Distances and Redshifts—Galaxies: Photometry—Methods: Statistical—Methods: Data Analysis

### 1. INTRODUCTION

The last decade has seen great advances in our understanding of the evolution of the Universe, primarily due to ground-breaking studies of the intermediate (Lilly et al. 1995b) and high redshift (Steidel et al. 1996) Universe. These "pencil beam" surveys probed to cosmological depths over quite modest areas, revealing the strong luminosity, morphological, and clustering evolution of the galaxy population over the last 12 Gyr. It was, however, recognized at the time that the small windows on the Universe provided by these surveys were

likely subject to substantial cosmic variance, in particular for measurements on the scale of the survey field sizes. This is epitomized by the Hubble Deep Field (HDF, Williams et al. 1996) images, which are "skewers" in redshift space, in which the ratio of transverse size (on the plane of the sky) to depth is  $< 10^{-3}$ . While allowing an unprecedented view of the high redshift Universe, essentially all studies based on the HDF alone have been dominated by cosmic variance.

In the last two years, the 2dF (Colless et al. 2001) and SDSS (York et al. 2000) surveys have provided us with the first reliable "local" ( $z \sim 0.1$ ) measurements of the galaxy luminosity function (Norberg et al. 2002b; Blanton et al. 2003), providing a crucial baseline reference for evolutionary studies. In addition, measurements of the galaxy correlation function in these surveys (Norberg et al. 2002a; Zehavi et al. 2002) have convincingly demonstrated luminosity-dependent clustering long seen at lower significance in smaller samples. These

<sup>1</sup> Visiting Astronomer, Canada-France-Hawaii Telescope, operated by the National Research Council of Canada, the Conseil nationale de recherche scientifique and the University of Hawaii.

<sup>2</sup> Visiting Astronomer, Cerro Tololo Inter American Observatory and Mayall 4-meter Telescopes, divisions of the National Optical Astronomy Observatories, which are operated by the Association of Universities for Research in Astronomy, Inc. under cooperative agreement with the National Science Foundation.

surveys finally overcame the cosmic variance issues that had plagued previous local surveys by sampling over  $10^3$  square degrees.

Contemporary with these local efforts, the development of wide-field mosaic CCD cameras has enabled deep imaging surveys covering fields hundreds of times larger than the HDF. Sensitive to galaxies at  $z \sim 1$  and beyond, these surveys have led to improved angular clustering measurements (e.g. Postman et al. 1998; McCracken et al. 2001) and the emergence and establishment of weak gravitational lensing as a powerful measure of the mass distribution in the Universe (for a review see Van Waerbeke and Mellier 2003). In fact, with current wide-field studies (e.g. Hoekstra et al. 2002; Van Waerbeke et al. 2002) the potential of weak lensing to map out the dark matter distribution is limited only by the systematic errors, including the assumed source and lens plane redshift distributions used to deproject the angular power spectrum. The primary goal of this paper is to provide accurate redshift distributions down to  $I_{AB} = 24$  and  $R_{AB} = 24.5$  for current and future weak lensing studies.

The Canada-France Deep Fields (CFDF) survey is a deep *UBVI* imaging survey which we have previously used to study the angular correlation function in  $30' \times 30'$  fields (McCracken et al. 2001) and the clustering properties of Lyman-break galaxies at  $z \sim 3$  (Foucaud et al. 2003). In this paper we describe the enhancements to the original survey, which consist of deep complementary *R* and *Z*-band imaging, as well as additional *B* and *I*-band imaging using the CFH12k mosaic CCD camera. We culled the full survey down to produce an extremely deep, highly uniform *UBVRIZ* sub-sample, dubbed the CFDF Photometric Redshift Survey (CFDF-PRS), which forms the basis of several evolutionary measurements of the galaxy population as a function of redshift. Future papers (Brodwin et al, in preparation) will present studies of the galaxy luminosity and correlation functions.

In this paper we focus on an accurate measurement of the galaxy redshift distribution from  $0 < z < 1.3$ . We introduce a novel iterative technique to extract the optimal redshift distribution using the full redshift likelihood functions for each galaxy. We present our binned redshift distributions along with parametrized fits to our results to aid weak lensing studies. Our results can also be used in the Limber deprojection of the angular correlation function over this redshift interval. Finally we devote a considerable portion of the paper to a discussion of the effects of cosmic variance in the current sample, and offer our suggestions for future measurements of  $N(z)$ .

The outline of this paper is as follows. Section §2 briefly describes the CFDF data, including new observations, and defines the subset used for photometric redshift estimation. Section §3 describes the photometric redshift algorithm used in the CFDF, including the use of the CFRS spectroscopic sample to optimize the redshift accuracy. Section §4 introduces the iterative Bayesian method of recovering the redshift distribution using the full redshift probability function for each galaxy. The convergence properties of the method are presented and tested in a detailed Monte Carlo simulation. In Section §5 we present the photometric redshift distributions, obtained using the iterative method, as a function of sample limiting magnitude in the CFDF down to  $I_{AB} = 24$  and  $R_{AB} = 24.5$ . We discuss the field-to-field variance and the theoretical expectations for our survey geometry, and compute median redshifts as a function of magnitude (with esti-

mates of both statistical and systematic errors). In Section §6 we present our complete redshift distributions in 0.5 magnitude bins. We also provide parametrized fits to our distributions, including absolute normalizations, with  $1-\sigma$  bootstrap-resampled errors. In Section §7 we briefly comment on the efficiency gain of photometric redshift surveys over traditional spectroscopy in statistical measurements of the evolution of large scale structure. Finally, in Section §8 we present our conclusions and summarize the advantages and caveats of the iterative method.

Most of our results are independent of cosmology. Where necessary we have assumed a concordance cosmology in agreement with the recent WMAP (Spergel et al. 2003) results  $\{\Omega_M, \Omega_\Lambda\} = \{0.27, 0.73\}$  and a Hubble constant  $h = 0.71$  where  $H_0 = 100h$ . All distances are expressed in comoving Mpc.

## 2. CANADA-FRANCE DEEP FIELDS

The Canada-France Deep Fields (CFDF) is a deep, multi-color imaging survey covering  $1 \text{ deg}^2$  (McCracken et al. 2001; Foucaud et al. 2003, hereafter CFDF1 and CFDF2, respectively). The acquisition, reduction, and verification of the astrometric and photometric integrity of the original *UBVI* data are described extensively in CFDF1. This first paper in the series also includes extensive completeness simulations showing that the survey is  $\sim 90\%$  complete to  $I_{AB} \leq 24$ . Deep *B<sub>AB</sub>* and *I<sub>AB</sub>* galaxy counts along with a detailed angular clustering analysis confirm the reliability of the data to at least this depth.

### 2.1. Supplementary **R** and **Z** Imaging

Photometric redshift simulations described elsewhere (Brodwin et al. 1999) indicated the need for additional *R*- and *Z*-band imaging to produce accurate photometric redshifts in the range  $z < 1.3$ . Further deep CFHT imaging was obtained in these bands, along with some additional *I* and *B* imaging to replace time originally lost to bad weather. We replaced the UH8k data with this superior, deeper CFH12k *I* and *B* data, since combining the two datasets would have degraded the excellent CFH12k seeing and cosmetic quality and while adding little in terms of depth. These data were reduced, stacked and calibrated using standard procedures (e.g. bias subtraction, flat fielding, fringe removal, geometric distortion correction), carefully adapted to mosaic CCD imaging as described in CFDF1 and Brodwin (2003).

New catalogues for this work were generated using the  $\chi^2$  technique of Szalay et al. (1999) from the highest quality photometric bands in each field, with a maximum omission of 2 non-adjacent filters and the requirement of at least *B*-band to *Z*-band wavelength coverage.

As explained below, the various magnitude limited galaxy samples studied in this paper were selected using total magnitudes as measured by the SExtractor (Bertin and Arnouts 1996) MAG\_AUTO parameter, whereas the photometric redshifts are computed using  $2.5''$  diameter aperture magnitudes.

### 2.2. Photometric Redshift Sample

As explained in CFDF2, *U*-band imaging only exists in 2.5 of our  $4 30' \times 30'$  fields. In addition, data in one of the eight UH8k CCDs with which the original data was taken is not science grade, due to bad charge transfer efficiency. Limiting the survey to those regions containing 6-band photometry, and excluding the regions masked due to bright (and saturated) stars, scattered light, remnant cosmetic defects that sur-

TABLE 1. FINAL PHOTOMETRIC SENSITIVITIES IN THE CFDF-PRS.

Field	R.A. (2000)	Dec. (2000)	Area (deg <sup>2</sup> )	Band	5 $\sigma$ /2.5'' (AB mags)
03hr	03:03:00	+00:09:00	0.17	U	25.17
				B	25.41
				V	25.04
				R	25.15
				I	25.04
				Z	24.26
14hr	14:17:10	+52:24:43	0.18	U	25.88
				B	25.33
				V	25.04
				R	25.21
				I	24.51
				Z	24.47
22hr	22:17:48	+00:17:13	0.10	U	25.96
				B	25.23
				V	25.18
				R	25.42
				I	25.36
				Z	24.65

vived the median stacking, and the aforementioned unreliable CCD, resulted in a final CFDF-Photometric Redshift Survey (CFDF-PRS) area of 0.45 deg<sup>2</sup>. Although such conservative cuts remove over half of the original survey area from the PRS, the remaining data is of very high quality and uniformity, and has the wavelength coverage necessary for robust photometric redshifts. The final photometric sensitivities for the CFDF-PRS are presented in Table 1.

### 3. PHOTOMETRIC REDSHIFT ALGORITHM IN THE CFDF-PRS

In order to estimate photometric redshifts and calculate the redshift probability distributions needed for the present study as well as the luminosity and clustering analysis of future CFDF papers (Brodwin et al. in preparation), an empirical template fitting algorithm was implemented. With our images convolved to a common (worst) seeing in each field (between 1.0'' – 1.3''), we compared 2.5'' diameter aperture *UBVRIZ* fluxes to a set of empirical templates SEDs. We adopted the Coleman et al. (1980) empirical SEDs, supplemented by the Kinney et al. (1996) SB2 and SB3 starburst SEDs as the basis templates in our algorithm. This combination of templates has been shown to span the range of galaxy properties in the HDF from 0 <  $z$  < 6 (Benítez 2000; Fernández-Soto et al. 2002). Fifteen interpolates of these basis spectra were used to improve the redshift resolution. Galaxy reddening is naturally incorporated into our empirical templates, as they are each composite spectra from numerous galaxies with varying levels of extinction.

A maximum likelihood method (ML) was used to produce the redshift likelihood surface for each object, as a function of redshift  $z$  and spectral type  $T$ :

$$\mathcal{L}(z, T) \propto \exp[-\chi^2(z, T)/2] \quad (1)$$

where

$$\chi^2(z, T) = \sum_i^{N_f} \frac{[f_i - A F_i(z, T)]^2}{\sigma_i^2}. \quad (2)$$

Here  $A$  is a simple scaling factor chosen to minimize  $\chi^2$  for each template,  $F_i(z, T)$  is the flux of the empirical galaxy template  $T$  through the  $i$ -th filter at redshift  $z$ ,  $f_i$  and  $\sigma_i$  are the object's fluxes and 1- $\sigma$  flux errors in the  $i$ -th filter and the sum runs over the  $N_f$  filters. The overall normalization of the likelihood surface is arbitrary. The likelihood surface is projected to a simple function of redshift by maximizing with respect to  $T$  at each redshift (i.e. using the ML of the best-fit template SED at each  $z$ ).

It is preferable to project the likelihood functions in this way rather than marginalize over all templates since the correct relative template density is unknown. As an extreme example, suppose we use only the 4 standard Coleman et al. (1980) templates (i.e. E, Sbc, Scd, Im) and add 100 interpolates between Sbc and Scd. In measuring the redshift of an elliptical galaxy our likelihood surface will contain some probability at each of these interpolated templates, albeit at a far lower level than the maximum likelihood at the correct redshift for the elliptical template. It is evident that integrating over all the templates produces a redshift likelihood function strongly dependent on the sampling of the template space. It can even lead to catastrophic failures when the integral of this low level probability surpasses the maximum likelihood of the  $z$ - $T$  surface.

This code was tested extensively with public HDF data and using the hundreds of CFRS spectroscopic redshifts in our fields. The latter sample allowed a novel form of calibration of the method to significantly improve the redshift accuracy (see below). In the HDF, the simple ML redshifts matched the excellent results in the literature (Benítez 2000; Fernández-Soto et al. 2002), with redshift dispersions of  $\sigma_z \sim 0.08(1+z)$  over the full redshift range  $0 < z < 6$  and only one “catastrophic error” (for details see Fernández-Soto et al. 2002).

#### 3.1. Calibration Using CFRS Spectroscopic Redshifts

The accuracy of photometric redshift estimation can be improved using a spectroscopic training set (e.g. Csabai et al. 2003). Yee (1998) pointed out the danger in applying such a modified algorithm on galaxy populations with different properties (e.g. apparent magnitude, color, redshift) than those of the calibrators. The danger is minimized in the template fitting algorithms (as compared with simple fitting functions), but not eliminated as illustrated by the recent SDSS (Csabai et al. 2003) photometric redshift results. In that study, the template SEDs, modified to better match the colors of the spectroscopic training set, were considerably less accurate for the higher redshift CNOC2 galaxies.

Despite the fact that the CFRS galaxies do in fact span nearly the full redshift range of interest for our filter set ( $z \lesssim 1.3$ ), we have opted not to modify the template SEDs to better match the CFRS spectroscopic redshifts. The much deeper CFDF-PRS samples galaxies 10 times fainter without loss of sensitivity to objects with weak or absent emission lines. The selection functions between the calibrators and the main sample are therefore quite different.

We have instead improved the photometric calibration using the spectroscopic sample as a novel kind of calibrator. Using only CFRS galaxies with the most secure spectroscopic redshifts (confidence class 3 and 4), we have a training set of 329 galaxies between  $0 \leq z \leq 1$  and  $18.5 \leq I_{\text{AB}} \leq 22.5$  (where the bright limit is imposed by the saturation limit of the CFDF-PRS).

We examined the magnitude residuals of the best-fitting

template at the correct (spectroscopic) redshift, as a function of the color of the galaxy. As an example, if all galaxies, regardless of redshift or spectral type, showed a residual,  $\Delta m$ , in some band, that would suggest that there was a zero point offset of  $\Delta m$  in that filter. If  $\Delta m$  was correlated with the color of the objects, that would indicate an error in the effective wavelength (the origin of which is inaccurate filter transmission or QE curves). In practice such color terms were negligible as expected, whereas small but significant zeropoint offsets were found in several filters. These offsets are caused, in part, by band-to-band seeing variations not fully removed when we convolve our images in each filter to the same seeing. Such residual seeing variations would manifest as zeropoint offsets. Almost all calculated offsets were less than 0.1 mag, the largest being 0.12 mag. An example is shown in Figure 1 for the  $R$  filter in the 03hr field.

This optimal calibration produces photometric redshifts with identical error properties in all three CFDF-PRS fields, as shown in Figure 2. The redshift dispersion, in the common measure in which the error increases as  $(1+z)$  is  $\sigma_z/(1+z) = 0.042$  for galaxies within the  $3\sigma$  limits of the distribution (includes over 92% of the galaxies). The direct dispersion for this sample is  $\sigma_z = 0.062$ . Defining a catastrophic failure of the photometric redshift method as one in which  $|z_{\text{ph}} - z_{\text{sp}}| \geq 1.0$ , the catastrophic fraction is 3.7%, or roughly half of the galaxies rejected from the statistical analysis.

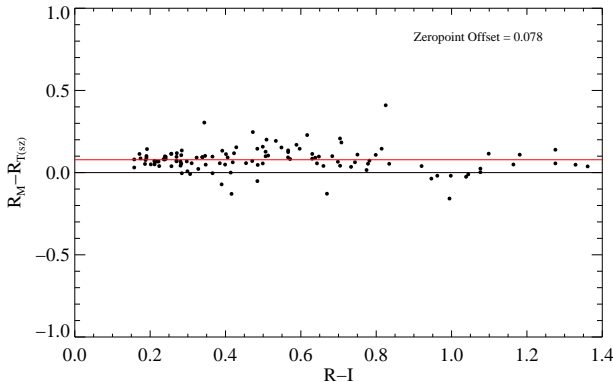


FIG. 1.— Residuals between the measured  $R$  magnitudes and the best-fitting template SEDs redshifted to the spectroscopic redshifts versus galaxy color. This technique essentially identifies the optimal photometric zero point and the effective wavelength in each broadband filter, using the CFRS galaxies as photometric standards. In this 03hr  $R$  band plot, the zeropoint offset is  $\sim 0.08$  magnitudes.

It is important to stress that no bias was introduced to the CFDF-PRS through the use of the CFRS spectroscopy. The true redshifts were used to transform the CFRS galaxies present in the CFDF-PRS into photometric standards, which were in turn used to tweak our zeropoints. Given the spectroscopic redshifts, the process is completely internal to the CFDF-PRS photometry, and results in optimal photometric redshifts for our depth and wavelength coverage.

### 3.2. Photometric Redshift Accuracy for $I_{\text{AB}} > 22.5$ Galaxies

In order to test the accuracy of photometric redshifts at magnitudes fainter than the CFRS data, we added a scaled version of each image in each field back to itself, with a positional offset larger than the full CFRS field. Care was taken to

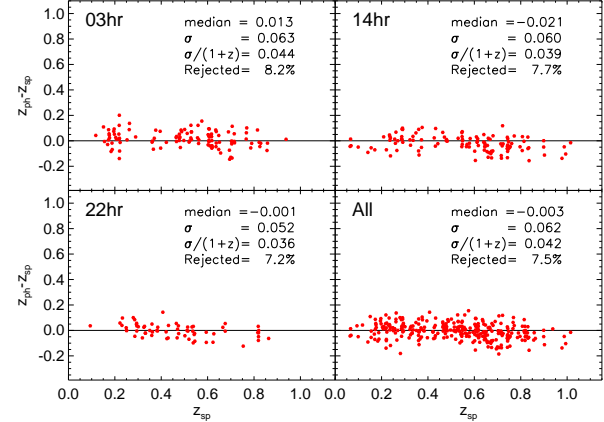


FIG. 2.— Residuals in photometric vs. spectroscopic redshift for the  $\sim 92\%$  of  $I_{\text{AB}} \leq 22.5$  CFRS galaxies that fall within the  $3\sigma$  limits of the distribution. The actual redshift dispersion for this sample is  $\sigma \sim 0.06$ . In the commonly used  $\sigma/(1+z)$  measure the dispersion drops to  $\sim 0.04$ .

ensure that the noise properties of the resulting images were identical to those of the original images. Specifically, in each field and filter we multiplied the original image by a scale factor,  $f_1$ , translated this scaled image by  $\sim 10'$ , and added it back to the original image. We then divided this new image by  $(1+f_1^2)^{0.5}$  to restore the original image's noise properties. The scale factor,  $f_1$ , is chosen such that in the final image CFRS galaxies with  $I_{\text{AB}} = 22.5$  are transformed into  $I_{\text{AB}} = 24$  objects (i.e. a 1.5 magnitude change  $\rightarrow f_1 \approx 0.2595$ ).

These fainter CFRS galaxies were photometered, and photometric redshifts were computed as above. The results, shown in Figure 3, demonstrate that while the increasing photometric error only modestly affects the redshift dispersion to  $I_{\text{AB}} \sim 24$ , the fraction of outliers increases to as much  $\sim 15\%$ . The catastrophic fraction roughly doubles to 8%. Clearly just using the maximum likelihood values of the redshift (described above) is problematic in statistical analyses of these faint galaxies.

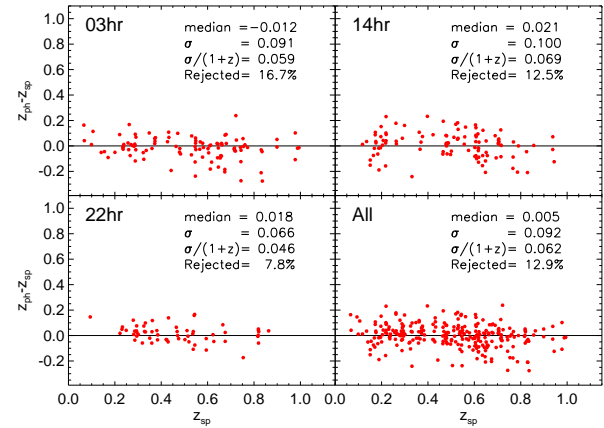


FIG. 3.— Residuals in photometric vs. spectroscopic redshift galaxies to  $I_{\text{AB}} \leq 24.0$ . The difference in imaging depths between the three CFDF-PRS fields is becoming apparent. In the 22hr field, the redshift dispersion and number of outliers is largely unchanged from the brighter sample in Figure 2. In contrast, the number of outliers has roughly doubled to 17% in the 03hr field. The redshift dispersions, in each field and overall, are still less than  $\sigma \sim 0.1$  to  $I_{\text{AB}} \sim 24.0$ .

### 3.3. Characterization of Catastrophic Errors

Catastrophic errors occur in every galaxy redshift survey, whether photometric or spectroscopic, at low signal-to-noise levels. As has been pointed out by Fernández-Soto et al. (2001), in many of the cases where the photometric and spectroscopic redshifts differed in the HDF, the catastrophic error was in the spectroscopic redshift (i.e. single emission lines were misidentified). With photometric redshifts, it is usually the Lyman  $\alpha$  and 4000 Å continuum breaks that are confused, although for galaxy photometry not containing one of these breaks the lack of a strong redshift signal alone can lead to wildly discrepant redshifts for the faintest galaxies.

We use the procedure described in the previous Section to produce fainter versions of the CFRS spectroscopic sample with the goal of characterizing the dependence of catastrophic errors on the signal-to-noise in the photometry. Figure 4 plots the observed catastrophic failure fraction, defined for simplicity as  $|z_{\text{ph}} - z_{\text{sp}}| \equiv \Delta z_{\text{cf}} \geq 1.0$  (filled symbols), vs. the various limiting magnitudes (top axis) to which we transformed the CFRS sample. As a reference for future photometric redshift surveys, we also plot the failure rate for catastrophic error definitions of  $\Delta z_{\text{cf}} \geq [0.5, 0.25]$  (open symbols).

The bottom axis shows how the catastrophic fraction depends on the corresponding signal-to-noise. The exposure times in the CFDF-PRS have been designed to produce roughly similar signal-to-noise levels in all filters for a typical galaxy. As such, the signal-to-noise axis, computed for the average  $I_{\text{AB}}$ -band depth, is nevertheless representative for all our filters.

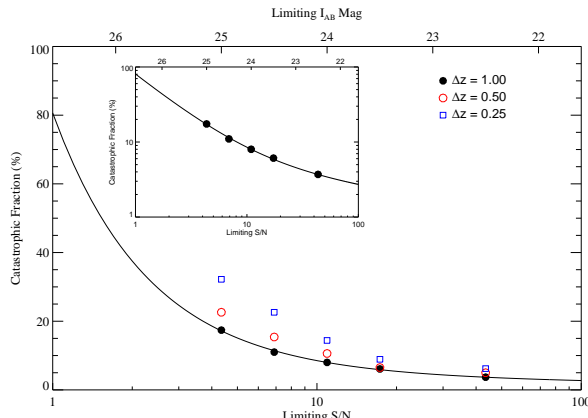


FIG. 4.— Catastrophic fraction as a function of minimum signal-to-noise in the CFDF-PRS. The points are derived from the fainter versions of the CFRS spectroscopic sample as explained in Section §3.2. The inset shows the same plot in the log-log space in which the empirical curve was fitted.

Obviously the curve in Figure 4, an empirical fit to the data (fitted in the log-log space shown in the inset), is specific to the CFDF-PRS, and cannot be blindly applied to other surveys. It depends on the number and wavelength coverage of the filters, the relative filter-to-filter photometric depths, and the photometric redshift algorithm (particularly the template SEDs). Nevertheless, for similar surveys the results are likely generic, in the sense that as the S/N approaches unity, the method breaks down completely. At the other extreme, there is an asymptotic catastrophic error fraction level of around 1%–2% which it will be difficult to transcend with the empirical galaxy templates used in this work.

For high signal-to-noise studies, like the HDF and UDF, the inclusion of rare object templates (e.g. ULIRGS, EROS, AGN, etc...) to the traditional elliptical, spiral and starburst templates of the present study may allow virtual elimination of catastrophic errors. However, for wide-field studies with more modest S/N levels, the addition of such rare templates may actually increase the catastrophic fraction since the data are not of sufficient quality to differentiate amongst all the templates. A minimum template basis spanning the full color range, as in the present study, is likely optimal at modest ( $\sim 10$ ) signal-to-noise.

To the CFDF-PRS limit of  $I_{\text{AB}} = 24$  there is little difference between the  $\Delta z_{\text{cf}} \geq 1.0$  and  $\Delta z_{\text{cf}} \geq 0.5$  catastrophic error fractions, whereas for  $z_{\text{cf}} \geq 0.25$  the catastrophic fraction begins to rise as the error level is approaching the tail of the photometric redshift error distribution. For ensemble statistical measurements like the redshift distribution, the relatively small catastrophic error fraction to  $I_{\text{AB}} = 24$  does not significantly affect our results, as demonstrated in the Monte Carlo simulation described below. Nevertheless, in Section §5.5 we will utilize the empirical fit of Figure 4 to try to estimate the potential systematic errors introduced to our results by catastrophic errors.

One caveat in using our method for estimating the occurrence of catastrophic errors with the  $I_{\text{AB}} < 22.5$  CFRS spectroscopic catalog is that high redshift galaxies near our faint magnitude limit are not explicitly included. Should they have spectral properties not spanned by our template set they could potentially introduce additional redshift degeneracies not identified by our Monte Carlo simulations. We are reassured by photometric redshift studies of the HDF (e.g. Fernández-Soto et al. 2001), which we have successfully reproduced with our code, that demonstrate that our templates do in fact span the full range of galaxy properties to  $z \sim 6$ , with the blue starburst templates becoming prominent above  $z \gtrsim 2$ . Certainly to  $I_{\text{AB}} < 24$  there is no indication of a population of galaxies with anomalous observed-frame optical SEDs. We explicitly test a subset of the faint, high redshift tail of the galaxy distribution in the next Section and find no discrepancy with the prediction of Figure 4.

### 3.4. Photometric Redshift Accuracy for $z \sim 3$ Lyman Break Galaxies

To test the photometric redshift algorithm at redshifts much higher than the CFRS, we have used the Steidel et al. (2003) spectroscopic sample of  $z \sim 3$  Lyman Break galaxies (LBGs) present in our 14hr field (their “Groth strip” field). The Steidel et al. (2003) photometry is fainter than in the CFDF-PRS and so we impose a minimum S/N limit of 3 in order to remove objects dominated by noise. As will be explained in Section §4.3.2 this is well below the S/N limit of 10 we will adopt in the CFDF-PRS analysis.

Figure 5 shows the redshift residuals for the 104 spectroscopic LBGs for which we compute photometric redshifts. This sample, being extremely limited in redshift space, is instructive in exploring the occurrence of catastrophic redshift errors. The filled symbols are well measured redshifts, whereas the open symbols, representing  $\sim 13\%$  of the sample, are catastrophic failures. Neglecting these, the photometric redshifts at  $z \sim 3$  have a dispersion of  $\sigma/(1+z) \sim 0.05$ .

We investigated the source of the catastrophic failures in this faint galaxy sample and concluded it stems from the difference in the  $U$  filters between the two surveys. The Steidel et al. (1996) bluer  $U_n$  filter allows selection of robust

LBG candidates at slightly lower redshifts than our  $U$  filter (in which the Lyman continuum break is only centered at  $z \sim 3.2$ ). The extremely faint  $z \sim 2.8$  Steidel et al. (2003) LBGs, without a strong continuum break in any of our filters, suffer a degeneracy between the  $z \sim 2.8$  starburst and  $0 \lesssim z \lesssim 0.5$  redder galaxy types. Approximately 20% of the faint  $2.7 \leq z \leq 3.0$  LBGs are misclassified as lower redshift galaxies.

Taken as a whole the LBG sample, at a limiting S/N of 3, has a lower failure rate than expected from Figure 4. This is not surprising since the Lyman Break selection criteria is designed specifically for broad-band photometric techniques. However the 20% failure rate for the  $z \lesssim 3.0$  LBGs that *don't* contain a strong photometric redshift signal are consistent with the prediction from Figure 4.

It is important to note that in this work, in addition to only using objects with  $S/N \geq 10$ , we are restricting ourselves to a redshift range which always contains the 4000 Å break. Nevertheless, rare bright high redshift objects can and do scatter down into our sample as expected. We address this systematic uncertainty in Section §5.5.

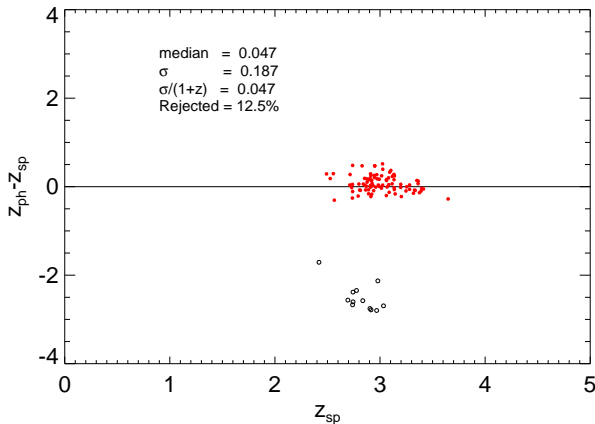


FIG. 5.— Residuals in photometric vs. spectroscopic redshift for 104 Steidel et al. (2003) Lyman Break galaxies with  $S/N \geq 3$  in the CFDF-PRS 14hr field. Excluding catastrophic errors (open symbols), the dispersion in redshift is  $\sigma/(1+z) \sim 0.05$ . The galaxies with catastrophic errors, roughly  $\sim 13\%$  of the sample, are clustered below  $z \sim 3$  where our filters do not straddle a strong continuum break.

### 3.5. Characterizing the Redshift Likelihood Functions Via Confidence Intervals

In Section §4 we will introduce a new method of calculating  $N(z)$  in photometric redshift surveys using the full redshift likelihood function for each galaxy. In this Section we characterize the error properties of our likelihood functions using the CFRS spectroscopic sample. Following Fernández-Soto et al. (2002) we define the 1, 2, and 3- $\sigma$  confidence intervals as those redshift regions which enclose the top 68.3%, 95.4%, and 99.7% of the area in our normalized redshift likelihood functions. At this point our likelihood functions have not been subjected to any prior (i.e there is equal a priori likelihood at all redshifts).

We found that convolving our likelihood functions with a Gaussian with  $\sigma = 0.04$  produced approximately normal confidence level statistics, as shown in Table 2, and has the beneficial effect of smoothing the likelihood functions. We note that the smoothing kernel is less than our redshift dispersion

TABLE 2. STATISTICS OF CONFIDENCE INTERVALS DERIVED FROM REDSHIFT LIKELIHOOD FUNCTIONS FOR CFRS SPECTROSCOPIC GALAXIES.

Confidence Interval	Observed Number	Expected Number
$\leq 1\sigma$	235/321	$219^{+16}_{-15}$
$\leq 2\sigma$	306/321	$306^{+15}_{-18}$
$\leq 3\sigma$	315/321	$320^{+18}_{-18}$
$> 3\sigma$	6/321	$0.9^{+2.2}_{-0.8}$

of  $\sim 0.06$  measured with the CFRS spectroscopic sample.

The confidence level statistics are quite consistent with a Gaussian error distribution within the Poissonian errors listed, although we place a slightly higher fraction of galaxies beyond the 3- $\sigma$  error limit. The 1- $\sigma$  confidence limit Poisson errors on the expected number of galaxies are computed using the Gehrels (1986) expressions valid for small numbers of events.

This exercise verifies the statistical validity of our redshift likelihood functions and of the analysis presented in Section §5 that incorporate them.

### 3.6. Star/Galaxy Separation

Most photometric redshift surveys rely on a simple morphological segregation of stars and galaxies since including model stellar SEDs in template fitting codes generally produces unreliable results (e. g. Chen et al. 2002; Firth et al. 2002). Morphological star/galaxy separation is only reliable at high signal-to-noise and at magnitudes bright enough so that galaxies are resolved. This limit is typically between  $21 \leq I_{AB} \leq 22$  for ground-based imaging.

We have instead devised an empirical, hybrid technique that incorporates both morphological and 4 color-color planes of information into a star/galaxy separation algorithm. We have tested the method and shown it to be reliable down to at least  $I_{AB} \sim 24$ . The algorithm is essentially a weighted voting scheme. The probabilities associated with each object's position in a concentration parameter-magnitude plane and 4 color-color planes are taken together to produce the overall likelihood of the object being a star. At brighter magnitudes the morphological information is more heavily weighted, whereas at the faint end the color information is much more important. Note that the colors are those of real (not model) stars, identified morphologically at  $Z_{AB} \leq 21$ . After substantial testing, we have adopted a concentration parameter of the difference of  $(0.75'' - 3'')$  aperture fluxes in our Z-band image in which the seeing varies from  $0.5'' - 0.7''$  in the three CFDF-PRS fields.

In each field, the expected number counts of stars are taken from the Bahcall and Soneira (1980) models, which we found matched the observed counts of morphological stars at bright magnitudes in all 3 CFDF-PRS fields. In each magnitude bin  $dm$ , if the Bahcall and Soneira (1980) model predicts  $N_*(dm)$  stars, we label as stars the  $N_*(dm)$  objects with the highest stellar likelihood in our hybrid method. The philosophy of the method may be summarized as follows. Given that the  $N_*(dm)$  stars are present in each magnitude bin, the idea is to rank the objects in terms of likelihood of being stars and removing the  $N_*(dm)$  most likely objects. It is, of course, a statistical correction and is strictly appropriate only for statistical analyses of the galaxy population. However, it is better

than simply ignoring the stars below the morphological classification limit.

We conducted two sets of tests to evaluate the reliability of the algorithm. A calculation of the angular correlation function confirmed that the objects classified as stellar are randomly distributed and that, as expected, the correlation amplitude of the remaining galaxies increased by  $1/(1-f)^2$ , where  $f$  is the stellar fraction of objects (e.g. Firth et al. 2002).

In addition, in the CFRS spectroscopic sample of 329 unsaturated galaxies to  $I_{AB} = 22.5$ , our method misclassifies only 4 galaxies as stars for an error rate of 1.2%. Figure 6 shows the cumulative distribution function of objects as a function of the stellarity vote for the CFRS sample. An advantage of

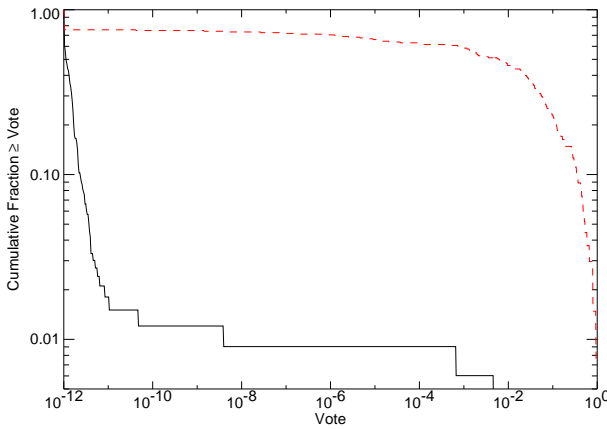


FIG. 6.— Cumulative distribution function of stellarity votes for CFRS stars (upper, dashed curve) and galaxies (lower curve). Ideal stars and galaxies should have votes of unity and zero, respectively. The strong segregation of stars and galaxies is apparent, with less than 2% of galaxies receiving votes above  $10^{-11}$  and over 60% of stars having votes above 0.001. The final classification depends on the votes of the objects in each magnitude bin. It is therefore possible for galaxies with anomalously high votes to nevertheless not be misclassified as stars.

this method is that only a small percentage of objects at faint magnitudes — the expected stellar fraction — are subjected to classification. Therefore the error rate is expected to remain constant or even drop down to the faintest magnitudes as the stellar to galaxy number counts ratio becomes negligible.

#### 4. METHOD: CONSTRUCTING OPTICAL PHOTOMETRIC REDSHIFT DISTRIBUTIONS

Several groups have published redshift distributions based on photometric redshifts in the Hubble Deep Field (e.g. Gwyn and Hartwick 1996; Sawicki et al. 1997; Fontana et al. 1999). Typically the best-fit photometric redshift is taken as that which maximizes a likelihood function, optionally subjected to a prior in Bayesian analyses (e.g. Benítez 2000). In the limit of narrow, singly-peaked redshift likelihood functions, this approach is a sensible one. Comparisons with spectroscopic redshifts in the HDF have convincingly demonstrated the accuracy and reliability of the photometric redshift method (e.g. Fernández-Soto et al. 2002) under the joint conditions of high quality photometry over a substantial wavelength baseline.

An open question regarding the photometric redshift method is how the signal-to-noise in the photometry affects the resulting redshift distributions. At present, due to the difficulty of obtaining spectra for  $AB(8140) > 25$  galaxies, 90% of HDF galaxies with spectroscopic redshifts have photome-

try with  $S/N \geq 100$  (Fernández-Soto et al. 2002). The photometric redshift technique has not been adequately tested at the lower S/N levels more common in ground-based imaging surveys. The method presented below addresses this issue in the CFDF-PRS and in anticipation of upcoming wide-field near-HDF depth imaging surveys (such as the CFHT Legacy Survey).

Detailed Monte Carlo simulations (described below) demonstrate that simple maximum likelihood photometric redshift methods increasingly fail to reproduce the underlying redshift distribution at lower S/N ( $\lesssim 20$ ). This Section describes a Bayesian method for recovering the underlying  $N(z)$  at still more modest S/N levels using the ensemble redshift information present in the data.

#### 4.1. Bayesian Photometric Redshift Distributions

As described in detail in Benítez (2000), Bayesian statistics provide a way to incorporate our knowledge about the galaxy distribution to improve the photometric redshift accuracy. This is accomplished through the use of priors on the simple likelihood functions, which by nature assume all redshifts are a priori equally likely. The prior converts the likelihood functions into true Bayesian redshift probability distributions which can be incorporated directly into cosmological studies in place of traditional spectroscopic redshifts (which, in general, can be thought of as approximately  $\delta$ -function redshift probabilities).

Specifically,

$$P(z, T) \propto P[z, T | N(z)] \times \mathcal{L}(z, T) \quad (3)$$

where  $\mathcal{L}(z, T)$ , the likelihood of measuring the observed colors for a galaxy of spectral type  $T$  at redshift  $z$ , is given in equation 1. In the Bayesian interpretation  $P[z, T | N(z)]$  is a prior, in this case the probability of drawing a galaxy with redshift  $z$  and type  $T$  from a redshift distribution  $N(z)$ . This prior, applied to the likelihood function, incorporates the basic fact that all redshifts are not a priori equally likely. As the goal here is to measure a statistical property of the galaxy population, namely its redshift distribution, requiring this information a priori may appear somewhat circular. However, we have devised an iterative scheme to recover the underlying redshift distribution and tested it in detailed Monte Carlo simulations.

#### 4.2. Direct summation of $N(z)$ and Iteration

Rather than adopting the simple maximum likelihood (ML) value of each galaxy redshift, we choose instead to directly sum up the normalized likelihood functions,  $\mathcal{L}^n$ , of each galaxy in the photometric sample. This would trivially produce the correct redshift distribution in the limit of spectroscopic (i.e.  $\delta$ -function) input redshifts. For photometric redshifts in the high signal-to-noise regime this method yields approximately the same result as collapsing the  $\mathcal{L}^n$  to the single maximum likelihood redshift since the  $\mathcal{L}^n$  are typically single sharp Gaussians. At fainter magnitude limits, the likelihood functions become broader and often develop multiple peaks as degeneracies between distinct templates at different redshifts arise with the increasing photometric error. With simple ML redshifts the derived  $N(z)$  is both too broad and has artificial peaks as significant numbers of galaxies are shifted between these degenerate redshifts. This is true as well of the first step of our iterative method:

$$N^0(z) = \sum_i \mathcal{L}_i^n(z) = \sum_i \frac{\mathcal{L}_i(z)}{\int_0^\infty \mathcal{L}_i(z) dz}. \quad (4)$$

This zeroth order redshift distribution,  $N^0(z)$ , is then used as the prior,  $P[z, T | N(z)]$ , in an iterative solution to equation 3. This prior uses the bulk information present in the galaxy colors to modify the raw likelihoods so as to minimize the degeneracies and, in effect, deconvolve the individual likelihood functions of the low S/N broadening effect. The resulting distribution serves as the first order prior,  $N^1(z)$ , and the procedure can be carried on to convergence, which, as shown in the following Section, is so rapid that additional steps are unnecessary.

Obviously the method breaks down at very low signal-to-noise. In the CFDF (and hence in the simulation described below) the sky background is brightest in the  $Z$ -band, limiting its depth compared with the other filters. This filter is doubly important as the red end of the wavelength baseline in the survey. At  $S/N \lesssim 10$  the method increasingly fails to converge to the input redshift distribution, underlining the importance of accurate Monte Carlo simulations to fully characterize photometric redshift surveys, and in particular, to determine their effective magnitude limit.

### 4.3. Convergence Properties

This method makes the assumption that a single prior is applicable to galaxies of all brightnesses and spectral types in a given sample. Ideally, each subclass of galaxies should have its own unique prior to optimally weight the simple likelihood functions. Obviously the a priori redshift likelihoods of large bright elliptical galaxies and faint blue Lyman break galaxies are quite different. The use of a single statistical prior, in this case the iteratively estimated redshift distribution, to describe a complete magnitude limited sample is obviously a rough approximation. However, with sufficient signal-to-noise in the photometry we demonstrate in the next few sections that it works surprisingly well.

This should not be mistaken to imply that redshifts of individual galaxies are uniformly improved using this method. It is the complete statistical redshift distribution that is demonstrably improved compared with that obtained via the standard method of collapsing the redshift likelihood function of each galaxy to a single maximum likelihood redshift.

#### 4.3.1. Formalism

Generalizing Equation 4 to include a single prior,  $P(z)$ , for a given sample

$$\mathcal{N}(z) = P(z) \sum_i \frac{\mathcal{L}_i(z)}{\int_0^\infty P(z) \mathcal{L}_i(z) dz}, \quad (5)$$

we see that the correct prior is the one for which  $\mathcal{N}(z) = N(z)$  (i. e. we recover the correct underlying redshift distribution). This leads to the following integral equation for  $P(z)$ :

$$P(z) = N(z) \left( \sum_i \frac{\mathcal{L}_i(z)}{\int_0^\infty P(z) \mathcal{L}_i(z) dz} \right)^{-1}, \quad (6)$$

which can be solved by iteration. Note that the functional form of the ideal prior depends on the likelihood functions, as expected since at very low S/N (reflected in the likelihoods) the method should fail. Viewing the prior as expressing a change of coordinates to a space in which the galaxy distribution is flat, one might expect the prior to be similar to  $N(z)$ . Therefore, we can use simulations to determine the redshift and S/N regimes in which taking  $P(z) = N(z)$  produces the

correct answer (i.e.  $\mathcal{N}(z) = N(z)$ ). It is straightforward to show that this requires

$$\eta \equiv \sum_i \frac{\mathcal{L}_i(z)}{\int_0^\infty N(z) \mathcal{L}_i(z) dz} = 1 \quad (7)$$

When this equation is satisfied, using  $N(z)$  as the prior is strictly correct. Although in general  $N(z)$  is not known a priori, assuming that  $N^0(z)$  from Equation 4 is a reasonable approximation to  $N(z)$ , one might still expect that

$$\eta^0 \equiv \sum_i \frac{\mathcal{L}_i(z)}{\int_0^\infty N^0(z) \mathcal{L}_i(z) dz} \approx 1 \quad (8)$$

is a valid convergence criterion.

#### 4.3.2. Convergence in Simulations

The convergence properties of the iterative method, studied in the Monte Carlo simulations described in the next Section, demonstrate its feasibility.

With sufficiently high signal-to-noise the iterative method converges after a single iteration. This is easily understood, as the likelihood functions are expected to be both narrow and overwhelmingly single-peaked. At very low S/N, the method ceases to converge and incorrect peaks in the iterative  $N(z)$  priors do not damp away, but remain constant or even increase in amplitude due to a kind of feedback loop. This shows the necessity of understanding the noise properties of photometric redshift surveys using accurate Monte Carlo simulations.

In the CFDF-PRS we set a conservative  $I$ -band S/N minimum of 10, based on a direct calculation of the convergence criteria of Equations 7 and 8 (shown in Figure 7), as well as the results of the Monte Carlo simulations described below. This corresponds to a limiting magnitude of  $I_{AB} \sim 24$ . The redshift range over which the method is reliable, apparent from Figure 7, is  $0.2 \lesssim z \lesssim 1.3$ , in very good agreement with the predictions for our filter set (Brodwin et al. 1999). In this

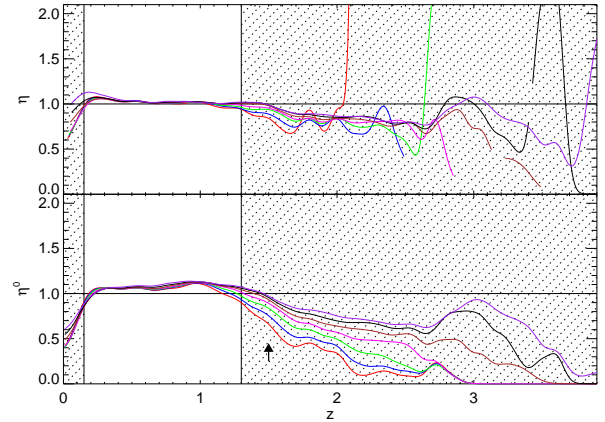


FIG. 7.—Convergence criteria  $\eta$  and  $\eta^0$  of Equations 7 and 8, calculated in the Monte Carlo simulation of Section 4.4. The unshaded region between  $0.2 < z < 1.3$  is identified as the most trustworthy for recovering the underlying redshift distributions for magnitude limited samples down to  $I_{AB} \sim 24$ . The curves represent samples down to limiting magnitudes of  $I_{AB} \leq 22.5$  (directly above arrow), rising to  $I_{AB} \leq 24$  in increments of 0.25 magnitudes. The curves in the top panel are undefined where  $N(z) = 0$  for bright magnitude limits at high redshift. The smoothing effect of the photometric redshift errors prevents this occurrence in the lower panel.

redshift range and to this magnitude limit the iterative method outperforms the simple ML method at reproducing the input redshift distributions in our simulations.

#### 4.4. Test of the Method: Monte Carlo Simulation

The iterative method described above was extensively tested in detailed Monte Carlo simulations. Briefly, model Universes were populated according to CNOC2 evolving luminosity functions (Lin et al. 1999) for early, intermediate and late spectral types, modified to produce a range of reasonable input redshift distributions to  $z > 3$ . These model galaxies were assigned colors using the empirical template set used in the CFDF photometric redshift code, ranging from the CWW Elliptical (Coleman et al. 1980) to the Kinney et al. (1996) SB2. Flux errors matching the *UBVRIZ* photometry in the CFDF fields were applied to these galaxies, and photometric redshift likelihood functions were computed for galaxies in an area of 0.5 deg<sup>2</sup>. A systematic error not accounted for in this simulation is the possible incompleteness of the adopted template SEDs with respect to the true range of galaxy properties. This was approximately accounted for following the method of Fernández-Soto et al. (2002) by convolving the computed redshift likelihood functions with a variable-width Gaussian.

$$\mathcal{L}^c(z) = \int_0^\infty dz' \mathcal{L}(z') G[z|z', \Sigma(1+z')] \quad (9)$$

where  $G$  is a normalized Gaussian (truncated at  $z < 0$ ) of median  $z'$  and  $\sigma = \Sigma(1+z')$ .  $\Sigma$  was set to 0.05 based on a detailed comparison with CFRS spectroscopic redshifts, as described in Section §3.1 (in fact, this is  $\sim 20\%$  larger than was found for the CFRS, but was adopted in a conservative vein).

##### 4.4.1. Simulation Results

In the interest of clarity we briefly recall the various methodologies our simulation was designed to test. The basic technique for computing redshift distributions consists of making a simple histogram of the best-fitting photometric redshifts for each galaxy. This is identical to taking the redshift that maximizes the likelihood function in likelihood-based fitting algorithms. We therefore dub this the *Peak-ML* method. Our new method, essentially a two-step iterative process, uses the full redshift likelihood function for each galaxy in computing  $N(z)$ . We therefore label it the *Full-RLF* iterative method (sometimes referred to simply as the *RLF* method for brevity). Redshift distributions were computed using both the Peak-ML method and the Full-RLF iterative method, and compared to the input  $N(z)$ . While the final iteration of the Full-RLF method is superior down to  $I_{AB} \leq 24.0$ , the improvement is most pronounced for the  $I_{AB} \leq 23.5$  sample, which we plot in Figures 8 and 9.

Figure 8 plots the redshift distributions obtained with the various methods. The filled and open circles represent the input (model) and Peak-ML redshift distributions, respectively. The dashed and solid lines show the Initial and Final iterations of the RLF method, respectively.

At first glance, all the methods appear to reproduce the input  $N(z)$  quite well. However, upon closer examination, it is clear that the Initial RLF  $N(z)$  is inferior to both the Peak-ML and the Final RLF distributions. On a qualitative level, we see that an incorrect secondary peak at  $z \sim 1.9$  draws galaxies away from the main peak at  $z \sim 0.7$ . This problem is most acute for the Initial RLF method, but is nevertheless evident in the Peak-ML points. The Final RLF method appears to suffer less from the effect of this photometric redshift degeneracy.

In fact, the trends observed with the different methods can be easily understood. Objects with little redshift ambiguity

(i.e. narrow, singly-peaked redshift likelihood functions) contribute to the different  $N(z)$  measures in the same, correct way. On the other hand, those objects whose redshift likelihood functions show a strong degeneracy (i.e. at least two similar peaks at distinct, aliased redshifts) contribute to  $N(z)$  in quite different ways in the above methods. In these cases the Peak-ML method usually selects the correct redshifts, although the catastrophic fraction increases with decreasing S/N. The main features of the input  $N(z)$  are therefore fairly well reproduced, although small peaks from the catastrophic errors will arise at specific aliased redshifts. The Initial RLF method, as the direct sum of the likelihood functions, will always underpredict the main  $N(z)$  peak as *all* the probability density of incorrect peaks at aliased redshifts is removed from it, leading to quite large peaks at the aliased redshifts. The Final RLF method, which uses the Initial RLF distribution as a prior, strongly suppresses these incorrect peaks using the information contained in the bulk of the galaxy sample (which is, on the whole, correct), bringing most of the ambiguous redshifts into line. A quantitative analysis demonstrates the superiority of the Final RLF method, and shows that it represents a significant improvement over the Peak-ML method.

To quantitatively assess the different methods we compare the resulting  $N(z)$  of each method to the input  $N(z)$  using a  $\chi^2$  test. To make a fair comparison, we integrate the iterative method curves over each Peak-ML redshift bin to produce a binned version of the iterative method for the  $\chi^2$  tests. The Initial RLF redshift distribution has a reduced  $\chi_\nu^2 = 14.5$  when compared with the input  $N(z)$ . The Peak-ML method, unsurprisingly, is much better, with  $\chi_\nu^2 = 4.02$ . It should be remembered that photometric redshift errors are not formally Gaussian. In fact in the low S/N regime, where multiple peaks arise, the error distribution is patently non-Gaussian, rendering impossible a direct confidence interval interpretation of the absolute  $\chi^2$  values. However, regardless of the nature of the photometric error distribution, reductions in  $\chi^2$  should indicate relatively better fits. In the Final RLF method the distribution no longer suffers from the effects of the redshift aliasing. The curve runs through (or very near) all the input  $N(z)$  data points, and the  $\chi_\nu^2$  drops to 1.25.

Figure 9 shows the individual contribution from each redshift bin to the total value of  $\chi_\nu^2$  for each method. The dramatic improvement from the Initial RLF (empty histogram) to Final RLF (densely filled histogram) is evident. The resulting  $N(z)$  has smaller deviations from the input distribution in every bin compared with the Peak-ML redshift distribution (sparsely filled histogram).

It is interesting to note that in this simulation the iterative method accurately recovers the redshift distribution outside the “guaranteed-convergence” redshift range of  $0.2 \lesssim z \lesssim 1.3$  discussed in Section §4.3.2. Various input redshift distributions and binnings have been investigated, with results consistent with those shown in Figure 8.

In addition to the  $\chi^2$  tests Kolmogorov-Smirnov (K-S) statistics were computed for all methods. The same pattern emerges, in which the Peak-ML method produces a redshift distribution more consistent with the input distribution than the Initial RLF method, but much less consistent than the Final RLF method. In this test the results are not impressive in either of the former two cases, with the somewhat better Peak-ML redshift distribution matching the input distribution at a probability of only  $10^{-3}$ . This is perhaps not surprising given the relatively high  $\chi^2$  test result. On the other hand, the final iteration of the Full-RLF method has a K-S probability

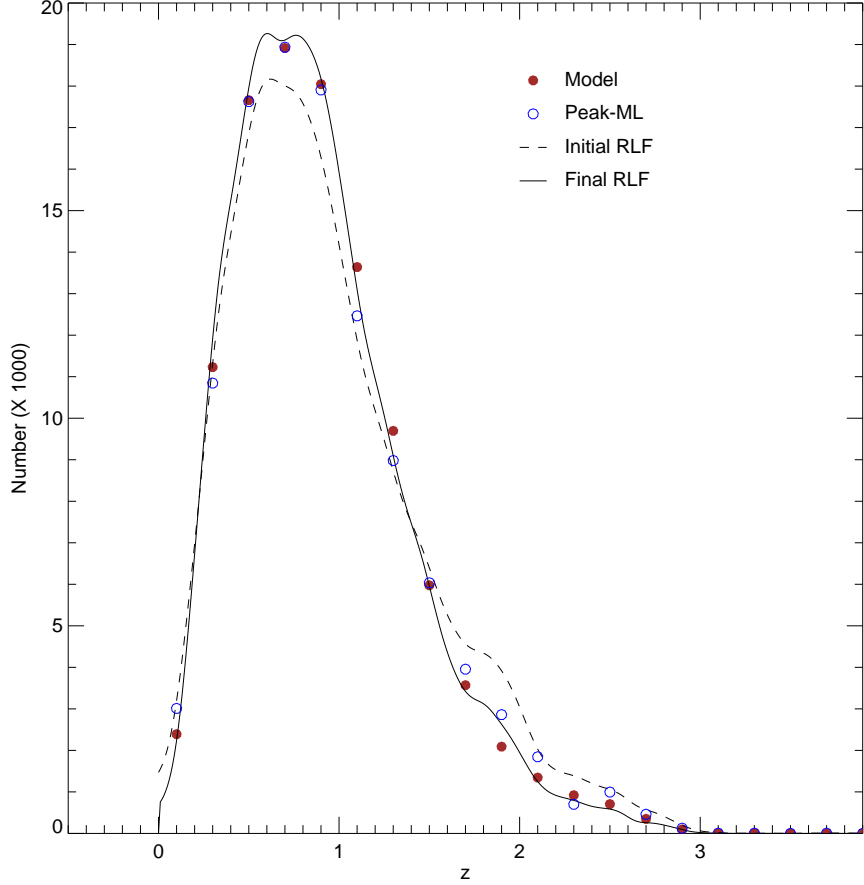


FIG. 8.— Results of Monte Carlo simulations testing Peak-ML (open circles), Initial RLF (dashed curve) and Final RLF (solid curve) methods for computing  $N(z)$  in a photometric redshift survey. The filled circles show the input (model)  $N(z)$ . The Peak-ML and Final RLF methods both recover the underlying  $N(z)$  quite faithfully, but the latter is in fact significantly better as discussed in the text and illustrated in Figure 9. Note how the aliased peak at  $z \sim 1.9$  in the Initial RLF iteration is strongly suppressed in the Final RLF distribution, reproducing the model  $N(z)$  better even than the Peak-ML method.

of 0.31 of matching the input distribution, which is the level of variation expected in a Poisson sampling of the underlying distribution.

##### 5. REDSHIFT DISTRIBUTIONS IN THE CFDF-PRS

The iterative method was applied to the CFDF-PRS data described in Section §2. The uniform magnitude selection is more representative of the general galaxy population than surveys that preselect their targets with color cuts (e. g. Coil et al. 2003), or have complicated spatial selection functions (e. g. Hogg et al. 2000). The  $I_{\text{AB}} \leq 24$  and  $R_{\text{AB}} \leq 24.5$  redshift distributions, presented in Section §5.2, are quite complementary with current lensing studies (Bacon et al. 2003; Hamana et al. 2003; Hoekstra et al. 2002; Maoli et al. 2001; Réfrégier et al. 2002; Van Waerbeke et al. 2002, 2001). At bright magnitudes our results can be compared directly with the CFRS redshift distributions (Crampton et al. 1995, hereafter CFRS5).

###### 5.1. Comparison with the CFRS

The three CFDF-PRS fields contain 3 of the 5 small fields in which the CFRS survey was carried out. We can therefore compare the redshift distributions of each field individually, as well as the aggregate results for the two surveys to the CFRS limit of  $I_{\text{AB}} = 22.5$ . It is important to stress that these surveys are completely independent. The imaging data

was taken with different cameras and filters, and the photometric calibrations are entirely independent. The CFRS magnitudes are isophotal, whereas in the CFDF we use SExtractor (Bertin and Arnouts 1996) total magnitudes (MAG\_AUTO).

Figure 10 compares the  $18.5 \leq I_{\text{AB}} \leq 22.5$  redshift distributions in each common field as well as for the sum of the fields. The solid curve is the Final RLF redshift distribution, the open circles represent the Peak-ML method, and the histogram is the original CFRS redshift distribution. The agreement in all three fields is remarkable, though not at all tautological. To this depth the CFDF-PRS contains over 20 times the number of CFRS galaxies in each field. Nevertheless the striking field to field differences in  $N(z)$  discussed in the CFRS persist in the present much larger survey. As discussed in CFRS5 these differences are not statistically significant for the small number ( $\sim 100$ ) of CFRS galaxies in each field when the effect of clustering is taken into account.

Following the method of CFRS5, we estimate  $N_C$ , the number of excess galaxies associated with each galaxy (including itself), for the CFRS spectroscopic sample to be  $N_C \sim 2$ . For a Poisson-distributed sample  $N_C = 1$  (i.e. the fluctuations in number density depend only on the individual galaxies), whereas the presence of small-scale clustering produces  $N_C > 1$ . This is just a reflection of the fact that correlated galaxies effectively come in clumps of  $N_C$  galaxies. Reducing

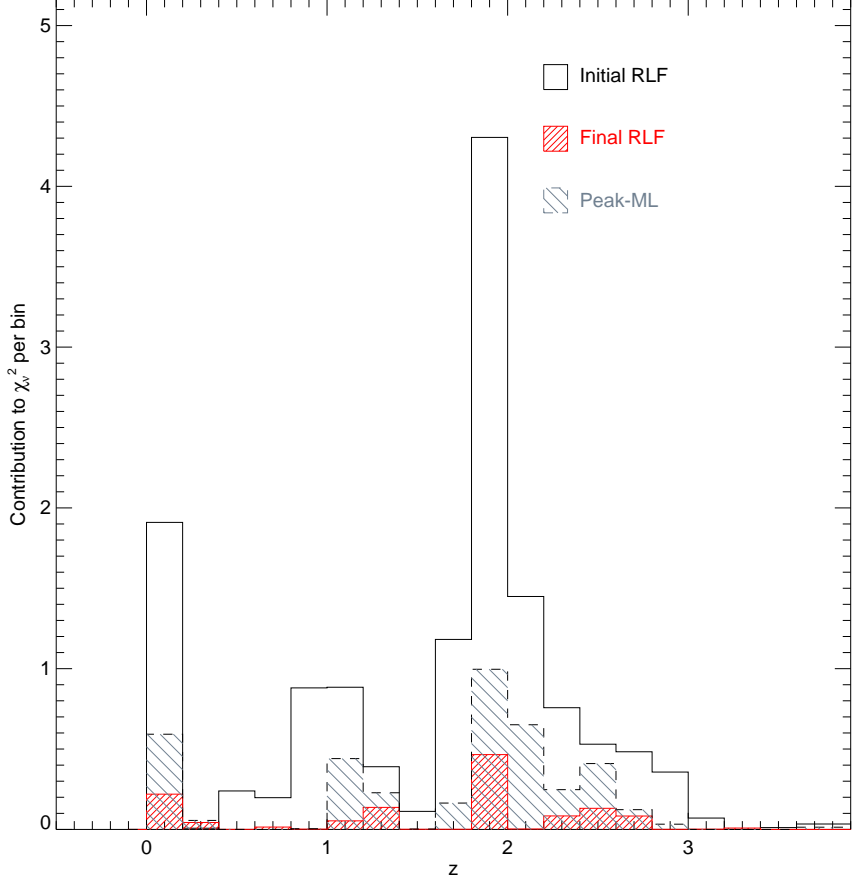


FIG. 9.— Contribution to  $\chi^2_{\nu}$  from each redshift bin for the Peak-ML (sparsely filled histogram), Initial RLF (empty histogram) and Final RLF (densely filled histogram) methods. Note the significant improvement over the Initial RLF method provided by both the Peak-ML and Final RLF distributions. The advantage of the Final RLF over the Peak-ML method is also apparent, as the differential  $\chi^2_{\nu}$  of the former is lower in each bin, often dramatically. The total  $\chi^2_{\nu}$  (i. e. summing over redshift) for these samples is {Initial RLF, Peak-ML, Final RLF} = {14.5, 4.02, 1.25}.

the number of independent galaxies in the CFRS by this factor, we find that the CFDF-PRS redshift distributions are entirely consistent with the original CFRS results, in each field and for the sum of the fields, despite the persistence of strong field-to-field differences (in particular between the 03hr and 22hr fields). It is perhaps surprising that the redshift distributions are not more homogeneous, given the half degree field sizes and a  $\sim 2000$  (comoving) Mpc baseline to the median redshift of the CFRS.

To test whether the field-to-field variations *within* the much larger CFDF-PRS itself are indicative of non-homogeneity of the galaxy distribution, we scaled the value of  $N_C$  found in the CFRS for the larger field size (integrating a  $\theta^{-0.8}$  correlation function) and spatial sampling (simple proportionality) of the CFDF-PRS, to arrive at  $N_C \sim 15$ . Reducing the number of independent galaxies by this factor, we find no convincing evidence of large scale anisotropies on the scales probed, beyond those attributable to small-scale galaxy correlations. However, those correlations do cause significant  $N(z)$  variations on at least 30' scales ( $\sim 30$  comoving Mpc at  $z = 1$ ).

The impressive agreement between the CFRS and the CFDF-PRS to  $I_{AB} \leq 22.5$  is a firm demonstration of the excellent control of systematic errors in the survey, as well as of the accuracy of the photometric redshift code and the iterative  $N(z)$  algorithm.

## 5.2. CFDF-PRS $I_{AB} \leq 24$ Redshift Distribution

Pushing beyond the CFRS limit, we present in Figure 11 the redshift distribution to  $I_{AB} \leq 24$  for the full CFDF-PRS. Once again the curve is the final iteration of the Full-RLF method, and the Peak-ML distribution is represented by the open circles. As expected, the main difference between these methods in the  $0.2 \leq z \leq 1.3$  convergence region (between the vertical dashed lines) is a relative paucity of objects in the Peak-ML method near the median redshift as these objects were scattered to one of the photometric redshift degeneracies at  $z \sim 1.5$  and  $z \sim 2.7$ . The Full-RLF partially corrects this effect, though a small fraction of objects remain clustered at these redshifts.

For comparison we plot in the inset the expected  $z \sim 3$  Lyman Break Galaxies to  $I_{AB} \leq 24$  from Steidel et al. (1999), along with the number of LBGs from CFDF2 to this depth, both scaled to a one degree field size. As explained in Section §3.4, the Steidel et al. (1996) filter set selects slightly lower redshift LBGs than in the present survey, leading to the small  $2.5 \lesssim z \lesssim 3.0$  peak of aliased redshifts. As we focus on the  $0.2 \leq I_{AB} \leq 1.3$  convergence region in this work, we refer the reader to CFDF2 for a more detailed discussion of the low redshift interlopers in the Lyman Break sample in the CFDF. We simply note that the LBG densities for both the Steidel et al. (1999) and CFDF2 samples lie roughly between the densities

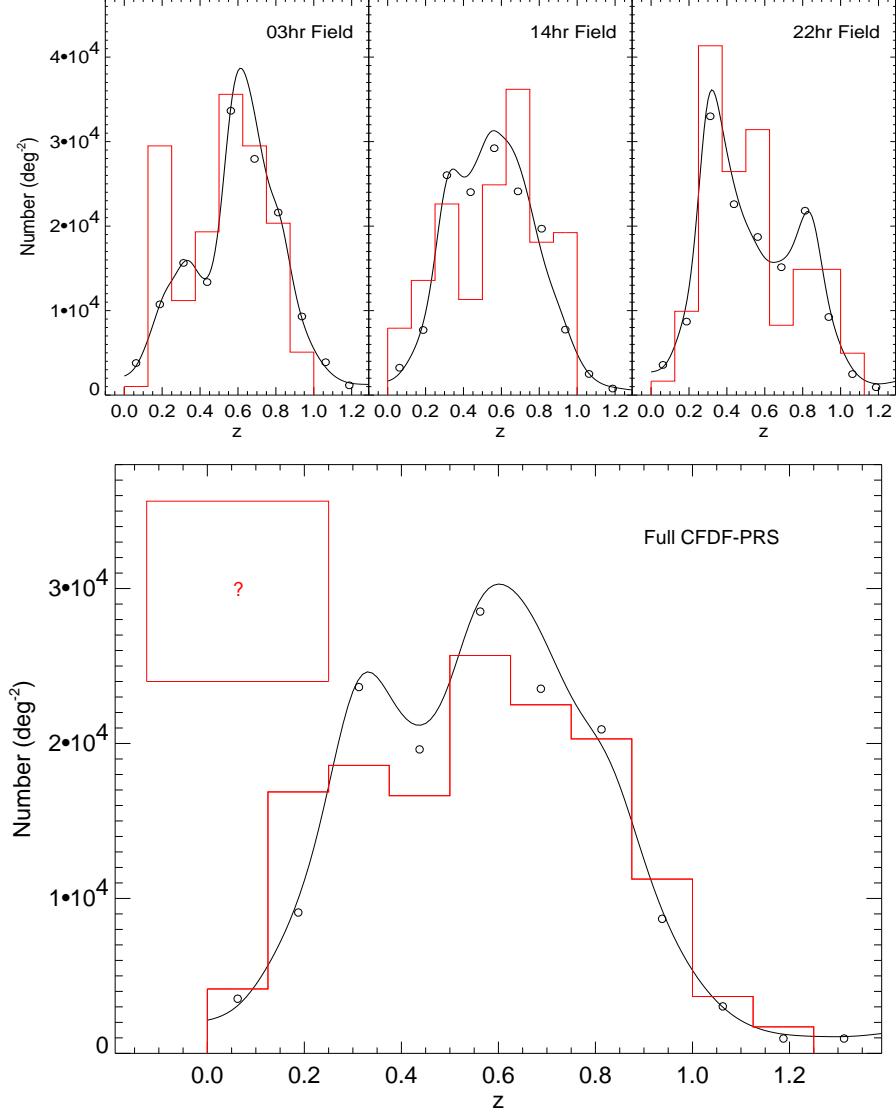


FIG. 10.—CFDF-PRS and CFRS redshift distributions over the common magnitude range  $18.5 \leq I_{AB} \leq 22.5$ . The curves are the Full-RLF final iteration, the points represent the Peak-ML distributions, and the histograms are from the CFRS. In the individual fields the CFRS number densities are scaled to the CFDF values, whereas in the combined fields we plot the CFRS distribution using their original normalization. The fraction of unidentified CFRS objects is represented by the box to the left of the peak. Stars have been removed from both samples.

of the Peak-ML and Full-RLF methods, offering a measure of proof that the present results are reasonable even at  $z \gg 1.3$ .

The distinct characteristics of each field, as well as the evolution from the brighter  $18.5 \leq I_{AB} \leq 22.5$  sample are discussed below. We first discuss the theoretical expectations concerning field-to-field variance for our survey geometry.

### 5.3. Theoretical Expectations for the CFDF-PRS Redshift Distribution

There is a considerable literature on the misleading effects of pencil beam surveys in measuring the 3D density distribution. When Broadhurst et al. (1990) measured an apparent periodicity in the Universe on  $128 h^{-1}$  Mpc scales, Kaiser and Peacock (1991), in a calculation of the 1D power spectrum in realistic survey geometries, concluded that in fact the statistical significance of the Broadhurst et al. (1990) result was quite low. The physical reason is that in projecting the 3D power spectrum down to 1D, power on scales of

the smallest survey dimension dominate the contribution to the large scale terms in the 1D power spectrum. Put another way, the 3D power transverse to the skewer (i.e. redshift) dimension is aliased on the scale of the field width. In fact Kaiser and Peacock (1991) showed that in pencil beam surveys, the clumpiness of galaxies so biases the sampling of the density field on the largest scales that only fluctuations of order unity would be significant on those scales.

With these issues in mind we compare the CFDF-PRS and HDF surveys with regard to the effect of cosmic variance. Current weak lensing studies typically rely on the HDF redshift distributions beyond the CFRS limit of  $I_{AB} = 22.5$ . The present work represents a significant improvement over the HDF to  $I_{AB} = 24$ , in particular in minimizing the effect of cosmic variance.

The CFDF-PRS is about 10% the volume of the 2dF at the median redshifts of the respective surveys. The HDF, in comparison, is 0.1% of the 2dF volume. To  $z = 1.3$  the CFDF

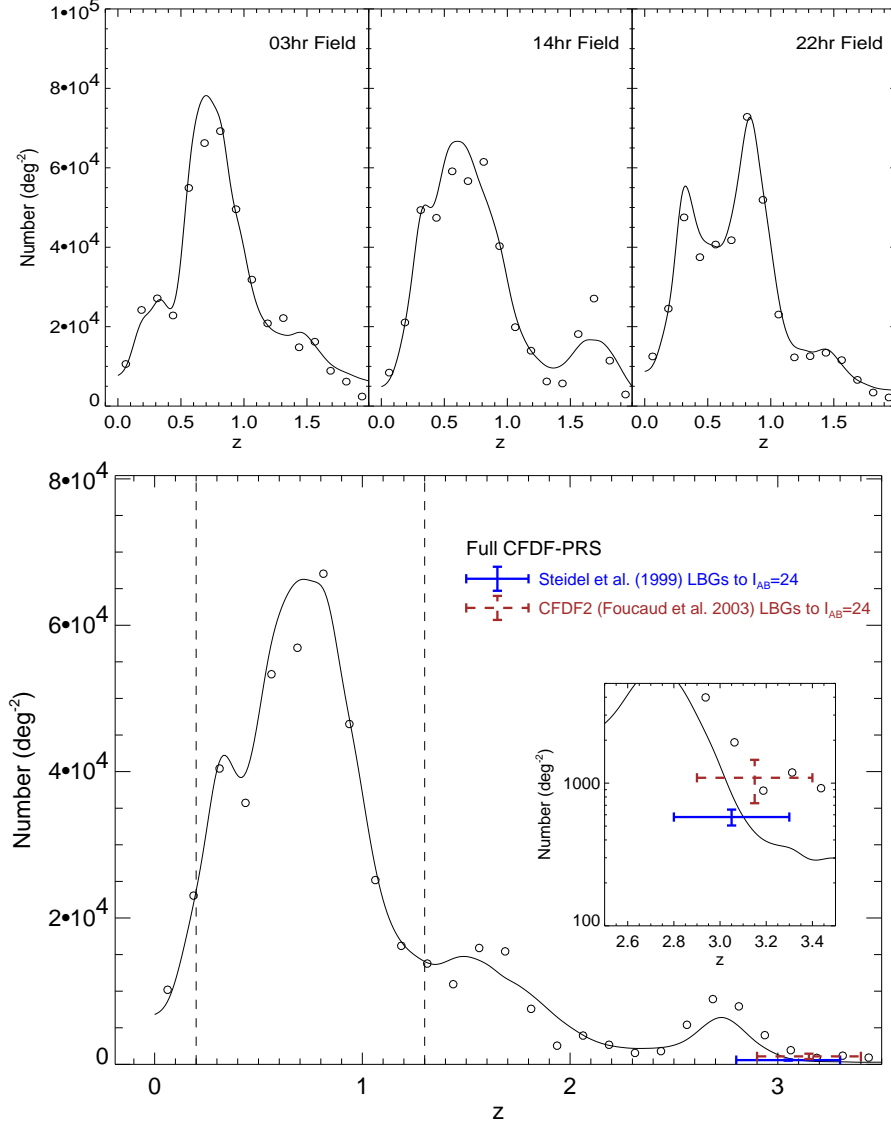


FIG. 11.—CFDF-PRS redshift distribution over magnitude range  $18.5 \leq I_{AB} \leq 24.0$ . The solid curve and empty circles represent the Final RLF and Peak-ML redshift distributions, respectively. Also plotted are the Steidel et al. (1999) and CFDF2 LBG counts (dashed error bar) integrated to  $I_{AB} = 24$  for comparison. The horizontal error bars represent the redshift sensitivity ranges of the respective LBG samples, whereas the vertical error bars show the  $1-\sigma$  errors in the integrated counts.

survey fields are 35 Mpc (comoving) across, compared to 3 Mpc for the HDF. With clustering largely limited to scales  $\lesssim 15$  Mpc, the effects of cosmic variance should be substantially lowered in the CFDF compared with the HDF. In fact the persistence of field-to-field variations to  $I_{AB} = 24$  in the CFDF-PRS (discussed in the next Section), while not indicative of large scale inhomogeneities in the Universe, are nevertheless significant for weak lensing studies. They are a strong confirmation that redshift distributions from HDF-sized fields are of extremely limited use, being totally dominated by cosmic variance (e.g. Somerville et al. 2003), and that even with much larger fields, averaging over multiple lines of sight is necessary. We minimally accomplish this with our three widely-separated fields, but more would be ideally required. Nevertheless, the CFDF-PRS redshift distributions represent a substantial improvement over the HDF in terms of area, volume and, of course, limiting the effect of cosmic variance.

#### 5.4. Evolution of $N(z)$ with Survey Depth

Comparing Figures 10 and 11, we see several trends in the transition from the CFRS depth to the CFDF-PRS limit of  $I_{AB} \sim 24$ . As expected, the  $z > 1$  sample grows as a fraction of the general population, from  $\sim 9\%$  to  $\sim 30\%$ , while the median redshift increases from  $\langle z \rangle \sim 0.6$  to  $\langle z \rangle \sim 0.8$ . Despite the smoothing effects of photometric redshift errors, discrete structures in redshift space are still clearly seen. We give a brief description of the evolution of these structures in each field with survey depth.

##### 5.4.1. 03hr Field (RA: $03^h 03^m 00^s$ DEC: $+00^\circ 09' 00''$ )

The 03hr field has considerable structure at  $0.6 \lesssim z \lesssim 0.7$ , including a probable cluster near the middle of the field. This is confirmed in the CFRS spectroscopic catalog which contains at least two physical associations of galaxies, each with about 15 galaxies within  $dz \leq 0.025$  of systemic redshifts of

$z \sim 0.605$  and  $z \sim 0.702$ . Interestingly, the CFRS did not cover the probable cluster (it being outside their survey area), but its presence strongly influenced the large scale structure they observed in this field. In the CFDF-PRS these two redshift space structures influence the redshift distribution in this field down to  $I_{AB} = 24$ , resulting in a relative paucity of galaxies at  $0.3 \lesssim z \lesssim 0.5$ , compared with the other fields and with the combined redshift distribution.

In a complementary medium deep XMM survey, Waskett et al. (2003, in preparation) discuss the X-ray sources present in the 03hr and 14hr CFDF fields.

#### 5.4.2. 14hr Field (RA: $14^h 17^m 10^s$ DEC: $+52^\circ 24' 43''$ )

The 14hr field (Groth Strip) is one of the best studied extragalactic fields (e.g. Groth et al. 1994; Lilly et al. 1995a; Steidel et al. 2003). It is the most normal, in some sense, of our three fields. The picket-fence structure observed in the CFRS has averaged out with the thirtyfold increase in area provided by the CFDF-PRS, leaving a relatively smooth, single-peaked, roughly Gaussian redshift distribution for  $z \leq 1.3$ . This distribution does not change appreciably in shape to  $I_{AB} = 24$ , aside from steady increases in median redshift and number density. However, at  $z \sim 1.8$  we observe a second peak arise in  $N(z)$  as we push to fainter magnitudes. Visual inspection of the galaxies involved indicates nothing unusual — they are entirely likely to be at the photometric redshift. However as this peak is outside our trusted redshift range of  $0.2 \leq z \leq 1.3$  we defer a detailed study of it until wide-field infrared imaging or spectroscopic redshifts are available.

The DEEP2 (Davis et al. 2003) redshift survey is targeting this field with the aim of obtaining 5000 redshifts to  $I_{AB} < 24.5$ . As such, it will perform a valuable check on the results presented here.

#### 5.4.3. 22hr Field (RA: $22^h 17^m 48^s$ DEC: $+00^\circ 17' 13''$ )

The 22hr field is perhaps the most interesting of the three. There is a large overdensity at  $z \sim 0.3$  observed in both the CFRS and the CFDF-PRS to the CFRS limit of  $I_{AB} \leq 22.5$ . Between  $22.5 \leq I_{AB} \leq 24$  the situation changes dramatically, and a broad peak at  $z \sim 0.8$  (the median redshift at this depth) emerges. The shape of  $N(z)$  in this magnitude interval is quite similar to that in the 03hr field, albeit at slightly higher redshift. As the sample selection deepens from  $18.5 \leq I_{AB} \leq 22.5$  to  $18.5 \leq I_{AB} \leq 24$  the relative sizes of the  $z \sim 0.3$  and  $z \sim 0.8$  peaks completely reverse. In addition, there is evidence for a substantial galaxy overdensity at  $z \sim 1$ .

The VIRMOS-VLT deep spectroscopic survey (VVDS Le Fèvre et al. 2003) will obtain tens of thousands of spectroscopic redshifts to  $I_{AB} < 22.5$  over  $3.6 \text{ deg}^2$  in this field. Given the relatively bright magnitude limit, it will be instructive to see whether this is sufficient area to obtain a redshift distribution unbiased by the  $z \sim 0.3$  structure seen in our data, and whether it will be deep enough to confirm the existence of considerable structure at  $z \sim 1$ .

#### 5.5. Median Redshifts in the CFDF-PRS

The extraction of cosmological parameters from weak lensing shear studies is, to good approximation, only sensitive to the median redshift of the galaxy population. While this is a fairly robust statistic, there are two sources of error which may bias the median in a photometric redshift survey such as CFDF-PRS. The first, cosmic variance, applies equally well to traditional spectroscopic surveys. It is a sort of random error, in the sense that it can be minimized by observing many

fields. With only  $n = 3$  fields the error on the directly measured field-to-field standard deviation is  $\sqrt{2/(n-1)} = 100\%$  (Pen et al. 2003), and as such is not particularly illuminating. Nevertheless it is expected to dominate the error budget.

The second source of error, catastrophic failures of the photometric redshift method caused by redshift aliasing in low S/N photometric data, is systematic in nature. The simulations of Section 4.4 indicate the redshift regime which is free of such aliasing ( $0.2 \leq z \leq 1.3$ ), and we in fact use this convergence region in fitting our redshift distributions in the next Section. However, catastrophic errors do take place outside this convergence region, as is clear from Figure 5, and we would like to investigate the effect of these errors on the median of the full sample.

We make two estimates of the systematic error due to redshift aliasing. The first, and most conservative, adopts the worst-case scenario that *all* redshifts outside the convergence region are untrustworthy, which from Section §3.4 we know is not the case. We compute the median omitting all objects outside the  $0 \leq z \leq 1.3$  convergence region, using two one-sided redshift cuts (i.e.  $z \geq 0.2$  and  $z \leq 1.3$ ) to estimate the asymmetric maximal systematic error possible in our survey. As an aside, this procedure formally computes only half the maximum theoretical error. To see this, note that applying the  $z \leq 1.3$  redshift restriction is equivalent to distributing the omitted high- $z$  galaxies exactly according to the distribution of the  $z \leq 1.3$  sample. But that's precisely the same, in terms of the median, as placing half of the high- $z$  galaxies at  $z = 0$  (or even just substantially below the median). Therefore the maximum theoretical error, corresponding to placing *all* of the  $z > 1.3$  galaxies below the median (i.e. corresponding to the case of 100% catastrophic errors outside our trusted redshift regime), is twice the error obtained from simply omitting them. However, given the impressive results for the  $z > 3$  sample in Figure 5, and the  $\sim 87\%$  overall success rate for the full LBG sample (which is significantly fainter than our survey limits), the systematic error from our redshift cuts is certainly the maximum possible error in *our* survey. In fact for the reasons just mentioned, it is almost certainly a gross overestimate.

A more realistic estimate of the systematic error is motivated from the catastrophic fractions observed in the CFRS in Section §3.3 as a function of limiting magnitude. We shift the catastrophic fraction of galaxies, as measured in Figure 4, from  $z \sim 0$  to  $z \sim 3$  and vice versa and recompute the median of the resulting distribution in each case to determine the magnitude of the systematic error on the actual survey median. These two cases account for what is seen in both the CFRS and Steidel et al. (2003) LBG samples, where objects are shifted back and forth between  $0 \lesssim z \lesssim 1$  and  $z \sim 3$ . Since the galaxies flow goes both ways, the effect of this aliasing ought to cancel out somewhat in statistical measures like the median. In addition we recall that the Final RLF method effectively reduces the redshift aliasing in the measured  $N(z)$ , using the bulk redshift information of the galaxy sample. Nevertheless we conservatively adopt as our best-estimate systematic error the full contribution of each catastrophic fraction (i.e. from shifting galaxies from  $z \sim 0$  to  $z \sim 3$  and vice versa). The CFDF-PRS  $I_{AB}$  and  $R_{AB}$  median redshifts, along with all of the error estimates are listed in Tables 3 and 4, respectively.

We also provide in these Tables median redshifts in differential (half) magnitude bins. Given these results, simple

apparent magnitudes cuts in future imaging surveys can be used as proxies for photometric redshift information in tomographic weak lensing studies.

The complete error on each median redshift consists of the random error (a quadrature sum of the bootstrap and field-to-field errors) as well as the best estimate of the asymmetric systematic errors. For the  $18.5 \leq I_{AB} \leq 24$  sample the median redshift is therefore  $\langle z \rangle = 0.77 \pm 0.049$  (random)  $^{+0.02}_{-0.01}$  (systematic), where we use angle brackets to denote the median. We include median redshifts for the  $24.0 \leq I_{AB} \leq 24.5$  and  $24.5 \leq R_{AB} \leq 25.0$  samples which are formally outside our trusted magnitude range for accurate photometric redshifts, as can be seen by the sudden rise in the systematic error for these samples. Nevertheless, as the median is a reasonably robust statistic and of significant value to weak lensing studies, we tentatively include these two medians for use until deeper photometric redshift surveys become available.

An important point to realize in interpreting Tables 3 and 4 is that the errors on the medians would persist in an ideal spectroscopic survey. The random error estimates are not specific to the photometric redshift method and would be unchanged for a similar spectroscopic sample. However, the spectroscopic redshift samples published to date do not approach the combination of field size, area and depth of the present survey, and have therefore been more affected by cosmic variance. The best-estimate systematic errors would remain non-zero for the faintest magnitude limits in a spectroscopic survey, as single line redshift identifications are inherently problematic and lead to catastrophic failures for as many as  $\sim 10\%$  of the galaxies (e.g. see Fernández-Soto et al. 2001). An additional systematic uncertainty, unique to spectroscopic surveys and quite difficult to estimate, is how spectroscopic incompleteness, most severe for galaxies with weak or absent emission lines, affects the measured  $N(z)$ .

As is clear from the Table, the field-to-field variance dominates the error budget in all cumulative (and most differential) magnitude ranges, and as such, the accuracy of the median redshifts in the CFDF-PRS is no worse than we had undertaken a more costly spectroscopic survey. In fact, for the reasons mentioned above it may be superior.

##### 5.6. Comparison to COMBO-17 and HDF Median Redshifts

In Figure 12 we compare our  $R$ -band median redshifts to those of the COMBO-17 (Brown et al. 2003) photometric redshift survey and the Cohen et al. (2000) spectroscopic survey of the HDF North. The median redshifts are plotted versus median  $R_{AB}$  magnitudes which we have tabulated alongside the various sample magnitude ranges in Table 4.

Although our bright limit of  $R_{AB} > 18.5$ , coupled with the relatively larger effect of cosmic variance at bright magnitudes makes a direct comparison non-trivial at  $R_{AB} \lesssim 20.5$  our results agree fairly well with, and are in fact intermediate between, these two other surveys. At fainter magnitudes these effects are minimized and the comparison becomes more straightforward. The agreement with both the COMBO-17 and Cohen et al. (2000) surveys is excellent for all  $R_{AB} \gtrsim 21$  within the quoted errors, which for the CFDF-PRS consist of the quadrature sum of the Poisson and field-to-field error terms. To be clear, the Cohen et al. (2000) errors are actually the 1st and 3rd quartile limits of the spectroscopic redshift distribution in each magnitude bin. While we agree with the Cohen et al. (2000) median redshifts within these conservatively large error limits, our fields clearly show

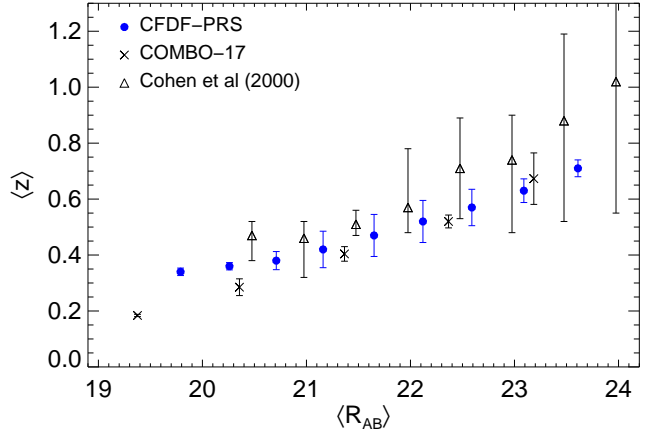


FIG. 12.— Median redshift vs. median  $R_{AB}$  magnitude in the CFDF-PRS (filled symbols). We have also plotted the results for the COMBO-17 survey (Brown et al. 2003) and the HDF North spectroscopic redshift survey of Cohen et al. (2000), both adjusted to AB magnitudes.

a lower median redshift at faint magnitudes, quite in line with the COMBO-17 results. In fact, given the strong agreement our results suggest that for ensemble statistical measurements of the galaxy population it is perhaps advantageous to employ only  $\sim 6$  broad-band filters (with spectral coverage from  $U$  through  $Z$  bands) and image more deeply rather than adopt a brighter medium band approach with  $\sim 15$  filters. While the photometric redshift error on individual galaxies is likely lower with the medium band survey strategy, broad-band photometric redshift surveys like the CFDF-PRS probe deeper down the luminosity function with little penalty on statistical measurements.

## 6. REPRESENTATIONS OF THE CFDF-PRS REDSHIFT DISTRIBUTIONS

In this Section we present our redshift distributions binned in magnitude and redshift, as well as in parametrized form in various magnitude ranges. It should be well noted that none of the main qualitative results of this paper change if simple maximum likelihood redshift (Peak-ML) values are used in place of the Final RLF described in Section §4. Although we have demonstrated that the iterated method produces optimal results, the slight differences in quantitative results are negligible compared to the field-to-field variance.

### 6.1. Binned Redshift Distributions

In Tables 5 and 6 we present the measured CFDF-PRS redshift distributions, digitized so as to present trustworthy information over all redshifts. Specifically, we digitize the Final RLF  $N(z)$  in redshift bins of  $\Delta z = 0.1$  for  $z < 1.3$  and much more broadly ( $\Delta z = 1.0$ ) at high redshift where the photometric redshifts are not as accurate. Our distributions are presented in 0.5 magnitude bins, which should enable other workers to construct redshift distributions for any sample in the range  $18.5 \leq I_{AB} \leq 24$ , with the obvious caveat that bright samples containing small numbers of objects have relatively larger uncertainties than deeper samples.

As an example, in Figure 13 we plot the binned distributions (filled symbols) for the CFRS depth of  $18.5 \leq I_{AB} \leq 22.5$  and the full CFDF-PRS depth of  $18.5 \leq I_{AB} \leq 24$  along with the full distributions (thin solid curves). The binned

TABLE 3.  $I_{AB}$  MEDIAN REDSHIFTS IN THE CFDF–PRS

Mag Range	$\langle I_{AB} \rangle$	$\langle z \rangle$	Random Errors		Potential Systematic Effects due to Redshift Aliasing			
			1- $\sigma$ Bootstrap	1- $\sigma$ Field-to-Field	$\Delta_{\text{best}}$ ( $z = 3 \rightarrow 0$ )	$\Delta_{\text{best}}$ ( $z = 0 \rightarrow 3$ )	$\Delta_{\text{max}}$ ( $z \leq 1.3$ )	$\Delta_{\text{max}}$ ( $z \geq 0.2$ )
$18.5 \leq I_{AB} \leq 20.5$	19.88	0.38	0.006	0.035	-0.00	0.00	-0.01	0.02
$18.5 \leq I_{AB} \leq 21.0$	20.36	0.43	0.006	0.065	-0.00	0.01	-0.01	0.03
$18.5 \leq I_{AB} \leq 21.5$	20.79	0.49	0.007	0.075	-0.00	0.01	-0.02	0.02
$18.5 \leq I_{AB} \leq 22.0$	21.23	0.54	0.006	0.070	-0.00	0.01	-0.01	0.02
$18.5 \leq I_{AB} \leq 22.5$	21.68	0.59	0.004	0.055	-0.00	0.01	-0.02	0.02
$18.5 \leq I_{AB} \leq 23.0$	22.11	0.64	0.004	0.031	-0.00	0.01	-0.03	0.02
$18.5 \leq I_{AB} \leq 23.5$	22.59	0.71	0.005	0.040	-0.01	0.01	-0.06	0.01
$18.5 \leq I_{AB} \leq 24.0$	23.11	0.77	0.005	0.049	-0.01	0.02	-0.09	0.02
<hr/>								
$18.5 \leq I_{AB} \leq 19.0$	18.76	0.30	0.010	0.023	-0.00	0.01	-0.01	0.03
$19.0 \leq I_{AB} \leq 19.5$	19.27	0.32	0.008	0.010	-0.00	0.00	-0.01	0.02
$19.5 \leq I_{AB} \leq 20.0$	19.79	0.39	0.011	0.023	-0.00	0.01	-0.01	0.02
$20.0 \leq I_{AB} \leq 20.5$	20.28	0.43	0.011	0.085	-0.00	0.01	-0.01	0.03
$20.5 \leq I_{AB} \leq 21.0$	20.79	0.52	0.010	0.072	-0.00	0.00	-0.01	0.02
$21.0 \leq I_{AB} \leq 21.5$	21.28	0.58	0.007	0.050	-0.00	0.01	-0.01	0.01
$21.5 \leq I_{AB} \leq 22.0$	21.78	0.63	0.007	0.040	-0.00	0.01	-0.02	0.01
$22.0 \leq I_{AB} \leq 22.5$	22.27	0.71	0.006	0.036	-0.01	0.00	-0.03	0.01
$22.5 \leq I_{AB} \leq 23.0$	22.77	0.78	0.007	0.031	-0.00	0.01	-0.06	0.02
$23.0 \leq I_{AB} \leq 23.5$	23.27	0.89	0.007	0.031	-0.01	0.01	-0.11	0.02
$23.5 \leq I_{AB} \leq 24.0$	23.78	1.03	0.008	0.061	-0.04	0.02	-0.23	0.03
$24.0 \leq I_{AB} \leq 24.5^1$	24.27	1.26	0.010	0.083	-0.13	0.04	-0.47	0.06

NOTE. — The best estimates of the upper and lower systematic errors ( $\Delta_{\text{best}}$ ) are computed using the catastrophic fraction as a function of magnitude from Figure 4. Errors of  $\pm 0.00$  are smaller than the photometric redshift resolution of 0.01.

<sup>1</sup>This is formally outside the range trusted for accurate photometric redshifts (see text).

TABLE 4.  $R_{AB}$  MEDIAN REDSHIFTS IN THE CFDF–PRS

Mag Range	$\langle R_{AB} \rangle$	$\langle z \rangle$	Random Errors		Potential Systematic Effects due to Redshift Aliasing			
			1- $\sigma$ Bootstrap	1- $\sigma$ Field-to-Field	$\Delta_{\text{best}}$ ( $z = 3 \rightarrow 0$ )	$\Delta_{\text{best}}$ ( $z = 0 \rightarrow 3$ )	$\Delta_{\text{max}}$ ( $z \leq 1.3$ )	$\Delta_{\text{max}}$ ( $z \geq 0.2$ )
$18.5 \leq R_{AB} \leq 20.5$	19.79	0.34	0.006	0.012	-0.00	0.01	-0.01	0.02
$18.5 \leq R_{AB} \leq 21.0$	20.26	0.36	0.005	0.012	-0.01	0.00	-0.01	0.02
$18.5 \leq R_{AB} \leq 21.5$	20.71	0.38	0.005	0.032	-0.00	0.01	-0.01	0.03
$18.5 \leq R_{AB} \leq 22.0$	21.16	0.42	0.005	0.065	-0.00	0.01	-0.01	0.03
$18.5 \leq R_{AB} \leq 22.5$	21.65	0.47	0.005	0.075	-0.01	0.01	-0.02	0.02
$18.5 \leq R_{AB} \leq 23.0$	22.12	0.52	0.005	0.075	-0.00	0.01	-0.02	0.02
$18.5 \leq R_{AB} \leq 23.5$	22.59	0.57	0.004	0.065	-0.00	0.01	-0.02	0.02
$18.5 \leq R_{AB} \leq 24.0$	23.09	0.63	0.005	0.042	-0.00	0.02	-0.04	0.02
$18.5 \leq R_{AB} \leq 24.5$	23.61	0.71	0.003	0.030	-0.01	0.02	-0.09	0.02
<hr/>								
$18.5 \leq R_{AB} \leq 19.0$	18.78	0.33	0.011	0.040	-0.00	0.01	-0.02	0.03
$19.0 \leq R_{AB} \leq 19.5$	19.29	0.32	0.009	0.023	-0.00	0.00	-0.01	0.02
$19.5 \leq R_{AB} \leq 20.0$	19.78	0.33	0.009	0.010	-0.00	0.00	-0.01	0.02
$20.0 \leq R_{AB} \leq 20.5$	20.29	0.37	0.009	0.021	-0.00	0.00	-0.01	0.02
$20.5 \leq R_{AB} \leq 21.0$	20.78	0.39	0.009	0.065	-0.00	0.01	-0.01	0.03
$21.0 \leq R_{AB} \leq 21.5$	21.27	0.44	0.009	0.068	-0.00	0.01	-0.00	0.03
$21.5 \leq R_{AB} \leq 22.0$	21.78	0.52	0.008	0.085	-0.00	0.01	-0.01	0.01
$22.0 \leq R_{AB} \leq 22.5$	22.28	0.55	0.006	0.076	-0.00	0.01	-0.01	0.02
$22.5 \leq R_{AB} \leq 23.0$	22.78	0.64	0.006	0.025	-0.00	0.00	-0.02	0.01
$23.0 \leq R_{AB} \leq 23.5$	23.28	0.73	0.006	0.023	-0.01	0.01	-0.05	0.01
$23.5 \leq R_{AB} \leq 24.0$	23.78	0.85	0.007	0.015	-0.02	0.01	-0.12	0.01
$24.0 \leq R_{AB} \leq 24.5$	24.28	1.01	0.009	0.040	-0.04	0.02	-0.24	0.04
$24.5 \leq R_{AB} \leq 25.0^1$	24.76	1.21	0.010	0.080	-0.11	0.03	-0.42	0.06

<sup>1</sup>This is formally outside the range trusted for accurate photometric redshifts (see text).

TABLE 5. BINNED  $I_{\text{AB}}$  CFDF-PRS REDSHIFT DISTRIBUTIONS

		$\langle I_{\text{AB}} \rangle_{\Delta m=0.5}$										
$z_l - z_h$	$z$	18.75	19.25	19.75	20.25	20.75	21.25	21.75	22.25	22.75	23.25	23.75
0.05–0.15	0.10	157	161	140	266	313	284	343	419	636	928	1703
0.15–0.25	0.20	320	390	362	533	726	750	956	1163	1395	1648	2594
0.25–0.35	0.30	638	905	869	1098	1316	1485	1702	2112	2080	2375	3058
0.35–0.45	0.40	281	547	921	1179	1404	1557	2007	2147	2207	2608	3255
0.45–0.55	0.50	79	181	638	1042	1718	1885	2787	2657	2961	3224	4384
0.55–0.65	0.60	48	78	387	968	2024	2665	3551	3735	4136	4544	5453
0.65–0.75	0.70	27	29	153	401	1229	2142	3355	4519	5260	6073	6573
0.75–0.85	0.80	10	10	44	162	562	1419	2743	4264	5526	7029	7506
0.85–1.95	0.90	3	6	20	75	238	771	1617	2967	4436	6511	7402
0.95–1.05	1.00	1	3	9	22	66	224	659	1506	2728	4899	6616
1.05–1.15	1.10	1	2	4	7	19	62	237	670	1448	2999	4870
1.15–1.25	1.20	0	1	3	5	10	32	125	377	990	2119	3764
1.25–2.25	1.75	0	1	2	2	5	16	62	199	512	1183	2373
1.75–2.75	2.25	6	4	5	8	8	11	40	85	204	507	1188
2.25–3.25	2.75	18	7	9	15	21	19	47	70	132	292	645
2.75–3.75	3.25	14	3	5	8	13	10	16	24	48	116	289
3.25–4.25	3.75	1	0	0	1	0	2	0	0	3	10	51
3.75–4.75	4.25	0	0	0	0	0	3	0	0	1	6	25

NOTE. — The redshift distributions are presented in constant 0.5 magnitude bins between  $18.5 \leq I_{\text{AB}} \leq 24$ , whereas the  $\Delta z = 0.1$  bin size in redshift is expanded to overlapping  $\Delta z = 1.0$  bins at  $z > 1.25$ . In each redshift bin the number of galaxies in the  $\Delta m = 0.5$  magnitude range is computed as  $N = \int_{z_l}^{z_h} N(z, m_l \leq I_{\text{AB}} \leq m_h) dz / \int_{z_l}^{z_h} dz$ , where  $m_l = \langle I_{\text{AB}} \rangle - 0.25$ ,  $m_h = \langle I_{\text{AB}} \rangle + 0.25$ , and the number densities,  $N$ , represent the CFDF-PRS survey area of  $0.4514 \text{ deg}^2$ .

TABLE 6. BINNED  $R_{\text{AB}}$  CFDF-PRS REDSHIFT DISTRIBUTIONS

		$\langle R_{\text{AB}} \rangle_{\Delta m=0.5}$											
$z_l - z_h$	$z$	18.75	19.25	19.75	20.25	20.75	21.25	21.75	22.25	22.75	23.25	23.75	24.25
0.05–0.15	0.10	128	150	183	168	318	279	306	408	429	743	1051	1956
0.15–0.25	0.20	230	303	432	443	642	782	794	1171	1125	1499	1722	2780
0.25–0.35	0.30	488	706	850	1017	1243	1553	1648	2088	2004	2279	2475	3240
0.35–0.45	0.40	340	410	605	929	1244	1658	1913	2239	2224	2571	2790	3410
0.45–0.55	0.50	92	144	222	630	1016	1802	2240	3031	3096	3109	3326	4204
0.55–0.65	0.60	43	93	114	302	650	1587	2755	3632	4382	4292	4591	5037
0.65–0.75	0.70	11	32	40	63	211	558	1615	2618	4373	5370	5893	6135
0.75–0.85	0.80	2	8	9	13	43	97	502	1339	2882	4900	6216	7061
0.85–1.95	0.90	1	3	3	3	14	22	133	575	1624	3232	5092	6597
0.95–1.05	1.00	0	2	1	2	8	5	40	208	698	1764	3377	5318
1.05–1.15	1.10	0	1	0	2	4	1	17	80	312	874	2077	3737
1.15–1.25	1.20	0	1	0	2	2	1	9	41	162	537	1496	2955
1.25–2.25	1.75	0	0	1	1	1	1	9	27	101	384	1031	2154
1.75–2.75	2.25	7	3	6	7	8	8	19	41	84	229	565	1240
2.25–3.25	2.75	20	8	10	13	20	16	27	45	68	139	297	696
2.75–3.75	3.25	14	7	5	7	12	9	12	15	27	44	126	341
3.25–4.25	3.75	1	1	0	1	0	0	1	1	2	2	23	77
3.75–4.75	4.25	0	0	0	0	0	0	2	1	0	0	3	15

NOTE. — All quantities are as in defined in Table 5, with the addition of the distribution for the  $24.0 < R_{\text{AB}} < 24.5$  bin in the final column.

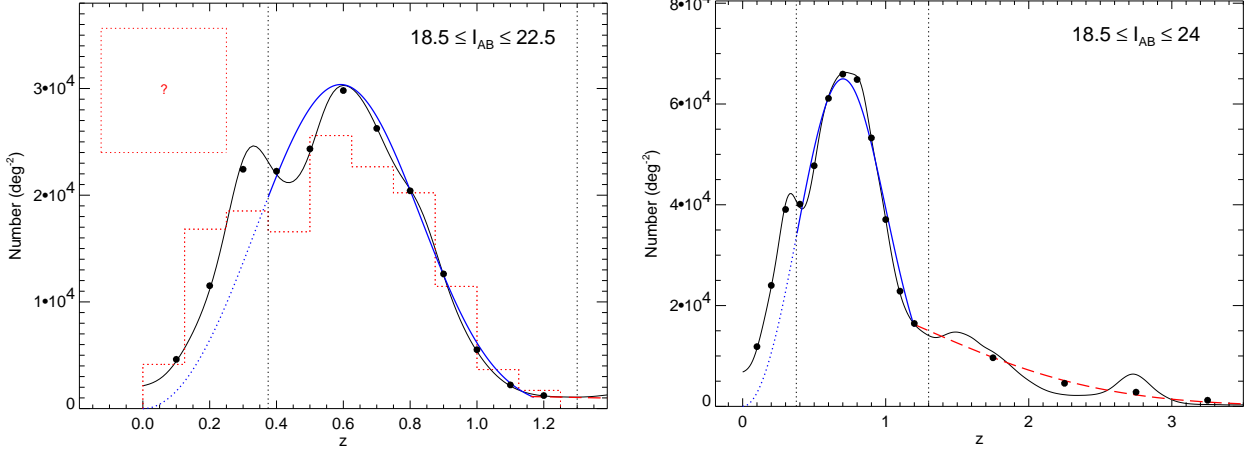


FIG. 13.—Binned distributions (solid symbols) and best-fit parametrizations plotted along with the  $18.5 \leq I_{AB} \leq 22.5$  and  $18.5 \leq I_{AB} \leq 24$  RLF redshift distributions (thin solid curves), scaled to 1 square degree. The solid thick line shows the best fitting parametrization of the main peak (Equation 10) at  $z \lesssim 1.2$  (represented as a dotted curve outside the fitting range, i. e. at  $z < 0.375$ ). At  $z \gtrsim 1.2$  the long-dashed curve is the best fitting model of the high redshift tail (Equation 11). The CFRS histogram is included for reference as the (dotted) histogram.

distributions accurately represent the data at all redshifts, although they are highly smoothed at  $z > 1.25$ . As such our distributions should be used in this form for precision (e. g. cosmic shear) measurements. For convenience we also provide parametrized fits to our distributions in the next Section.

### 6.2. Parametrizations of $N(z)$

Analytic fits of the form (Pen et al. 2003; Van Waerbeke et al. 2001)

$$N(z) = N_0 \frac{\beta}{z_0 \Gamma\left(\frac{1+\alpha}{\beta}\right)} \left(\frac{z}{z_0}\right)^\alpha \exp\left[-\left(\frac{z}{z_0}\right)^\beta\right] \quad (10)$$

were applied to our  $I_{AB}$  and  $R_{AB}$  redshift distributions in various magnitude ranges and the results are listed in Tables 7 and 8, respectively. We limit our fits to the redshift region  $0.375 \leq z \leq 1.3$ , i. e. we exclude the  $z \sim 0.3$  overdensity and fit the main single peak in each magnitude range.

Our fitting technique consists of minimizing the Kolmogorov–Smirnov distance  $D$  between the cumulative distribution functions of the model and Final RLF method redshift distributions over the allowed redshift range. The full three parameter fits  $[z_0, \alpha, \beta]$  have  $\alpha$  values very close to the commonly used value of 2.0, expected on geometric arguments for a flat average luminosity function. Without significantly compromising the accuracy of the fits, we therefore reduce the dimensionality of the analysis by setting  $\alpha \equiv 2.0$ . The  $1-\sigma$  single parameter errors in  $z_0$  and  $\beta$ , listed in the Tables, are estimated via 100 bootstrap resamplings (with repetitions) of the CFDF–PRS catalog, and subsequent recalculation of the redshift distributions using the Full–RLF method. The separately determined absolute number densities,  $N_0$ , along with bootstrap resampled errors are also listed in the Tables.

We found Equation 10 to be a sensible model for  $N(z)$  up to the CFRS depth ( $I_{AB} \sim 22.5$ ), but at fainter magnitudes it fails to simultaneously model the main  $z \lesssim 1$  peak and the increasing high redshift tail (at  $I_{AB} \lesssim 24$  the fraction of  $z > 1$  galaxies is approximately 30%). We therefore limit its application to the  $z \lesssim 1.2$  regime and fit the  $z \gtrsim 1.2$  tail of the

distribution with a decaying exponential,

$$N(z) = A_T \exp\left[-\left(\frac{z}{z_T}\right)^\gamma\right]. \quad (11)$$

Note that this equation is not fitted to the Final RLF  $N(z)$  but rather to the binned distributions calculated from Tables 5 and 6. The transition between Equations 10 and 11 is always very close to  $z \approx 1.2$ , but to produce a continuous parametrization should in general be taken to be the redshift at which the two parametrizations intersect.

For the high redshift tail the dominant errors are likely systematic in nature, coming from the photometric redshift algorithm operating in a redshift and magnitude regime where the convergence properties are highly uncertain. Without a large, deep spectroscopic comparison sample at  $1 < z < 3$  it is difficult to assess these errors in a meaningful way. In the present work we conservatively assign a maximum uncertainty of 50% to the fit in the  $z \gtrsim 1.3$  regime. Examples of the fits are shown in Figure 13 for the  $18.5 \leq I_{AB} \leq 22.5$  and  $18.5 \leq I_{AB} \leq 24.0$  samples. The solid, thick curve is the best fitting parametrization of the form of Equation 10 within the  $0.375 \leq z \leq 1.3$  fitting region, although it is likely correct at  $z < 0.375$  (dotted curve) due to the constraint at  $z = 0$ . At  $z \gtrsim 1.2$  the best-fit parametrization of the form of Equation 11 is represented by the long-dashed line. Taken together the full redshift range is well parametrized by these functions.

### 7. FUTURE MEASUREMENTS OF $N(z)$

In light of the preceding discussion, it is evident that in the redshift regimes in which multicolor imaging surveys have appropriate wavelength coverage and depth, the errors in photometric redshifts (conservatively  $\Delta z \sim 0.1$ ) are not the limiting factor in an accurate determination of  $N(z)$ . In addition, we have verified that the systematic errors inherent in the method are secondary to cosmic variance in the overall error budget.

The effect of cosmic variance similarly dominates the error budget of current and planned non-local spectroscopic surveys, at a level consistent with the present survey. This is due to the large contiguous field requirement of clustering analyses, among the primary goals in such surveys, which

TABLE 7. PARAMETRIZED FITS OF  $I_{AB}$  CFDF-PRS REDSHIFT DISTRIBUTIONS

Mag Range	$z \lesssim 1.2$				$z \gtrsim 1.2$		
	$N_0$	$z_0$	$\beta$		$A_T$	$z_T$	$\gamma$
$18.5 \leq I_{AB} \leq 24.0$	20785 (133)	0.790 (0.008)	2.788 (0.059)		11443	1.786	2.037
$19.0 \leq I_{AB} \leq 24.0$	20735 (141)	0.793 (0.009)	2.805 (0.067)		11472	1.783	2.039
$19.5 \leq I_{AB} \leq 24.0$	20625 (143)	0.800 (0.008)	2.852 (0.058)		11503	1.780	2.037
$20.0 \leq I_{AB} \leq 24.0$	20310 (135)	0.818 (0.009)	2.969 (0.074)		11557	1.776	2.033
$20.5 \leq I_{AB} \leq 24.0$	19800 (126)	0.840 (0.008)	3.123 (0.073)		11609	1.773	2.032
$21.0 \leq I_{AB} \leq 24.0$	18861 (141)	0.872 (0.007)	3.341 (0.074)		11695	1.770	2.031
$21.5 \leq I_{AB} \leq 24.0$	17569 (128)	0.902 (0.007)	3.529 (0.093)		11635	1.782	2.053
$22.0 \leq I_{AB} \leq 24.0$	15573 (120)	0.945 (0.008)	3.817 (0.121)		11672	1.776	2.043
$22.5 \leq I_{AB} \leq 24.0$	13046 (111)	0.978 (0.009)	3.904 (0.135)		11131	1.788	2.045
$23.0 \leq I_{AB} \leq 24.0$	9829 (90)	1.015 (0.008)	3.992 (0.122)		9383	1.837	2.074
<hr/>							
$18.5 \leq I_{AB} \leq 21.5$	3216 (169)	0.609 (0.010)	3.200 (0.096)	44	3.717	93.92	
$18.5 \leq I_{AB} \leq 22.0$	5205 (165)	0.644 (0.008)	3.175 (0.075)	109	3.460	14.55	
$18.5 \leq I_{AB} \leq 22.5$	7759 (186)	0.683 (0.009)	3.119 (0.068)	658	2.084	2.327	
$18.5 \leq I_{AB} \leq 23.0$	10979 (168)	0.720 (0.008)	3.048 (0.067)	2422	1.716	1.994	
$18.5 \leq I_{AB} \leq 23.5$	15293 (157)	0.760 (0.008)	2.941 (0.066)	5889	1.699	2.013	
$18.5 \leq I_{AB} \leq 24.0$	20785 (133)	0.790 (0.008)	2.788 (0.059)	11443	1.786	2.037	

NOTE. — The fits are for the CFDF-PRS survey area of  $0.4514 \text{ deg}^2$ . At  $z \lesssim 1.2$  the best-fitting parameters of Equation 10 are listed, along with bootstrap-resampled errors. At  $z \gtrsim 1.2$ , the parameters of fits of the form of Equation 11 are tabulated. We conservatively estimate the error in the high redshift tail to be 50%.TABLE 8. PARAMETRIZED FITS OF  $R_{AB}$  CFDF-PRS REDSHIFT DISTRIBUTIONS

Mag Range	$z \lesssim 1.2$				$z \gtrsim 1.2$		
	$N_0$	$z_0$	$\beta$		$A_T$	$z_T$	$\gamma$
$18.5 \leq R_{AB} \leq 24.0$	13446 (133)	0.662 (0.012)	2.601 (0.081)		2380	2.433	3.083
$19.0 \leq R_{AB} \leq 24.0$	13379 (121)	0.667 (0.011)	2.629 (0.073)		2415	2.407	3.034
$19.5 \leq R_{AB} \leq 24.0$	13288 (113)	0.673 (0.010)	2.659 (0.065)		2425	2.399	3.025
$20.0 \leq R_{AB} \leq 24.0$	13151 (113)	0.681 (0.012)	2.710 (0.081)		2447	2.384	2.999
$20.5 \leq R_{AB} \leq 24.0$	12859 (110)	0.701 (0.010)	2.837 (0.077)		2471	2.367	2.969
$21.0 \leq R_{AB} \leq 24.0$	12429 (122)	0.725 (0.010)	2.993 (0.087)		2507	2.343	2.927
$21.5 \leq R_{AB} \leq 24.0$	11659 (100)	0.761 (0.009)	3.232 (0.091)		2549	2.325	2.895
$22.0 \leq R_{AB} \leq 24.0$	10532 (113)	0.796 (0.010)	3.434 (0.115)		2591	2.302	2.881
$22.5 \leq R_{AB} \leq 24.0$	8896 (96)	0.848 (0.008)	3.812 (0.122)		2624	2.266	2.839
$23.0 \leq R_{AB} \leq 24.0$	6661 (78)	0.894 (0.010)	4.036 (0.153)		2532	2.228	2.770
<hr/>							
$18.5 \leq R_{AB} \leq 22.0$	2992 (170)	0.538 (0.011)	3.140 (0.111)	28	3.716	76.46	
$18.5 \leq R_{AB} \leq 22.5$	4607 (150)	0.567 (0.010)	3.116 (0.084)	70	3.670	45.30	
$18.5 \leq R_{AB} \leq 23.0$	6800 (150)	0.602 (0.011)	3.007 (0.083)	186	3.432	13.82	
$18.5 \leq R_{AB} \leq 23.5$	9632 (145)	0.634 (0.013)	2.825 (0.098)	612	2.982	5.643	
$18.5 \leq R_{AB} \leq 24.0$	13446 (133)	0.662 (0.012)	2.601 (0.081)	2380	2.433	3.083	
$18.5 \leq R_{AB} \leq 24.5$	18656 (146)	0.665 (0.012)	2.309 (0.060)	5930	2.337	2.778	

NOTE. — All quantities are defined as in Table 7. For the  $R_{AB}$  sample we also provide a fit for the  $18.5 \leq R_{AB} \leq 24.5$  magnitude range.

precludes the targeting of sufficient numbers of independent fields. An “optimal” spectroscopic survey strategy, of little use for studies of galaxy correlations, would contain many ( $N \sim 50 - 100$ ) deep, sparsely sampled fields to reduce the cosmic variance to the level of the systematic errors.

We believe this analysis clearly shows that multicolor photometric redshift surveys are equally capable of producing accurate measurements of  $N(z)$ , with three important advantages. The first is the lack of spectroscopic incompleteness, and hence no bias against objects with low star formation rates. Second, in an “optimal” survey with  $N$  fields, each multi-color imaging field, acquired at the same observational cost as a deep spectroscopic pointing, can have a field size

of order  $1^\circ \times 1^\circ$  with modern mosaic CCDs (e.g. Megacam). In addition to generating catalogues of  $\sim 10^5$  galaxies to  $I_{AB} \sim 25$ , this large field size produces a smaller cosmic variance *per field* as compared with a similar spectroscopic pointing. Finally, on a practical note, it is feasible from a cost perspective to obtain deep, multicolor imaging of a large contiguous area of sky several degrees on a side. Such a strategy allows many scientific analyses to be performed on a common data set, from 3-D clustering (using photometric redshifts) to weak lensing shear measurements, while producing a large number of effectively independent fields for the  $N(z)$  measurement. Subfields separated by  $\gtrsim 1^\circ - 2^\circ$  ( $\gtrsim 50 - 100$  Mpc at  $z = 0.75$ ) are virtually uncorrelated (in the sense that the cor-

relation function vanishes) and hence for an  $N \times N$  deg $^2$  box tiled with  $1^\circ \times 1^\circ$  pointings, roughly  $N^2/3$  to  $N^2/2$  pointings can be considered effectively independent.

The Wide Synoptic component of the ongoing CFHT Legacy Survey (CFHTLS) has such a survey geometry. Their filter set (wide  $u*$  plus SDSS  $g'r'i'z'$ ) will allow reliable photometric redshifts in a range similar to that in the present study, i. e.  $z \lesssim 1.3$ . It consists of three fields, one  $8^\circ \times 9^\circ$  and two  $7^\circ \times 7^\circ$ , allowing  $\sim 100$  quasi-independent samples of the galaxy distribution. In addition, these fields provide width to depth ratios of order  $\sim 15\%$ , improving on the CFDF-PRS by roughly the same factor that we improve on the HDF studies, and allowing a reliable measurement of power on  $\sim 500$  Mpc scales at  $z \sim 1$ . As such it will make the definitive measurement of  $N(z)$  for  $z \lesssim 1.3$  to  $AB \sim 24$ .

Extending the CFHTLS  $N(z)$  measurement to  $z > 1.3$  will require wide field infrared imaging, either from the ground with large field mosaic cameras (with degree field sizes), or from space where the absence of an overwhelming sky background allows efficient mapping with relatively small detectors (e.g. SIRTF).

## 8. SUMMARY

We have introduced a new technique to compute  $N(z)$  in which the full photometric redshift likelihood functions for each galaxy are incorporated to better reproduce the correct underlying redshift distribution. Direct summation of the likelihoods produces the Bayesian prior which accounts for the fact that all redshifts are not a priori equally likely. No information external to the survey is used in the Bayesian technique, rather we iterate within our own dataset. We have presented Monte Carlo simulations which prove the validity of the technique and demonstrate that it is a significant improvement over previous methods.

Our highly accurate photometric redshifts, calibrated using hundreds of spectroscopic CFRS galaxies, have typical dispersions of only  $\sigma/(1+z) \lesssim 0.06$  to  $I_{AB} = 24$  for  $z \leq 1.3$ . Our

large field sizes ( $30'$ ) and multiple, widely separated lines of sight produce redshift distributions far less affected by cosmic variance than previous surveys of similar depth. In particular, the Hubble Deep Fields, which are currently used to estimate the redshift distribution beyond the CFRS limit of  $I_{AB} = 22.5$  are completely dominated by cosmic variance. Our fields are 150 times bigger, and we sample a volume over 100 times larger than both HDFs combined. We compute  $I_{AB}$  and  $R_{AB}$  median redshifts, as a function of limiting magnitude and in differential magnitude bins, with an error budget consisting of bootstrap resampled random errors, field-to-field variance and an empirical estimate of the systematic errors due to photometric redshift aliasing. We present our  $I_{AB}$  and  $R_{AB}$  redshift distributions in tabular form and provide parametrized fits with errors estimated from bootstrap resampling.

Finally we point out that with photometric redshifts as accurate as in the CFDF-PRS cosmic variance alone currently dominates the error budget in measurements of  $N(z)$ . Sparsely sampled photometric or spectroscopic redshift surveys containing dozens of independent fields will be required to significantly improve upon our results. The CFHTLS Wide Synoptic survey plans to do this, using photometric redshifts in three large contiguous fields, which contain  $\sim 100$  statistically independent samples of the galaxy distribution.

We are grateful to Chuck Steidel for making his spectroscopic data available to us prior to publication, Chris Pritchett for observing some of our CFH12k data and Frank Valdes for assistance with MSCRED. MB would like to thank Ue-Li Pen, Henk Hoekstra, Barth Netterfield, and Peder Norberg for useful discussions. CP was supported by the Zwicky Prize fellowship program at ETH-Zürich. MB acknowledges support from the National Sciences and Engineering Research Council and the Ontario Graduate Scholarship program, as well as ETH-Zürich where much of this research was carried out.

## REFERENCES

Bacon, D. J., Massey, R. J., Refregier, A. R., and Ellis, R. S. 2003, *MNRAS*, **344**, 673

Bahcall, J. N. and Soneira, R. M. 1980, *ApJS*, **44**, 73

Benítez, N. 2000, *ApJ*, **536**, 571

Bertin, E. and Arnouts, S. 1996, *A&AS*, **117**, 393

Blanton, M. R., et al. 2003, *ApJ*, **592**, 819

Broadhurst, T. J., Ellis, R. S., Koo, D. C., and Szalay, A. S. 1990, *Nature*, **343**, 726

Brodwin, M. 2003, PhD thesis, University of Toronto

Brodwin, M., Lilly, S., and Crampton, D. 1999, in *ASP Conf. Ser. 191, Photometric Redshifts and the Detection of High Redshift Galaxies*, ed. Weymann, R. J. et al. (San Francisco: ASP), 105

Brown, M. L., Taylor, A. N., Bacon, D. J., Gray, M. E., Dye, S., Meisenheimer, K., and Wolf, C. 2003, *MNRAS*, **341**, 100

Chen, H., et al. 2002, *ApJ*, **570**, 54

Cohen, J. G., Hogg, D. W., Blandford, R., Cowie, L. L., Hu, E., Songaila, A., Shopbell, P., and Richberg, K. 2000, *ApJ*, **538**, 29

Coil, A. L., et al. 2003, *ApJ*, submitted (astro-ph/0305586)

Coleman, G. D., Wu, C.-C., and Weedman, D. W. 1980, *ApJS*, **43**, 393

Colless, M., et al. 2001, *MNRAS*, **328**, 1039

Crampton, D., Le Fevre, O., Lilly, S. J., and Hammer, F. 1995, *ApJ*, **455**, 96 (CFRS5)

Csabai, I., et al. 2003, *AJ*, **125**, 580

Davis, M., et al. 2003, in *Proceedings of the SPIE, Vol. 4834, Discoveries and Research Prospects from 6- to 10-Meter-Class Telescopes II*, ed. Guhathakurta, P., 161

Fernández-Soto, A., Lanzetta, K. M., Chen, H., Pascarelle, S. M., and Yahata, N. 2001, *ApJS*, **135**, 41

Fernández-Soto, A., Lanzetta, K. M., Chen, H.-W., Levine, B., and Yahata, N. 2002, *MNRAS*, **330**, 889

Firth, A. E., et al. 2002, *MNRAS*, **332**, 617

Fontana, A., et al. 1999, *A&A*, **343**, L19

Foucaud, S., McCracken, H. J., Le Fèvre, O., Arnouts, S., Brodwin, M., Lilly, S. J., Crampton, D., and Mellier, Y. 2003, *A&A*, in press (astro-ph/0306585, CFDF2)

Gehrels, N. 1986, *ApJ*, **303**, 336

Groth, E. J., Kristian, J. A., Lynds, R., O'Neil, E. J., Balsano, R., Rhodes, J., and WFPC-1 IDT 1994, *BAAS*, **26**, 1403

Gwyn, S. D. J. and Hartwick, F. D. A. 1996, *ApJ*, **468**, L77

Hamana, T., et al. 2003, *ApJ*, in press (astro-ph/0210450)

Hoekstra, H., Yee, H. K. C., and Gladders, M. D. 2002, *ApJ*, **577**, 595

Hogg, D. W., Cohen, J. G., and Blandford, R. 2000, *ApJ*, **545**, 32

Kaiser, N. and Peacock, J. A. 1991, *ApJ*, **379**, 482

Kinney, A. L., Calzetti, D., Bohlin, R. C., McQuade, K., Storchi-Bergmann, T., and Schmitt, H. R. 1996, *ApJ*, **467**, 38

Le Fèvre, O., et al. 2003, *A&A*, submitted (astro-ph/0306252)

Lilly, S. J., Hammer, F., Le Fevre, O., and Crampton, D. 1995a, *ApJ*, **455**, 75

Lilly, S. J., Le Fèvre, O., Crampton, D., Hammer, F., and Tresse, L. 1995b, *ApJ*, **455**, 50

Lin, H., Yee, H. K. C., Carlberg, R. G., Morris, S. L., Sawicki, M., Patton, D. R., Wirth, G., and Shepherd, C. W. 1999, *ApJ*, **518**, 533

Maoli, R., Van Waerbeke, L., Mellier, Y., Schneider, P., Jain, B., Bernardreau, F., Erben, T., and Fort, B. 2001, *A&A*, **368**, 766

McCracken, H. J., Le Fèvre, O., Brodwin, M., Foucaud, S., Lilly, S. J., Crampton, D., and Mellier, Y. 2001, *A&A*, **376**, 756 (CFDF1)

Norberg, P., et al. 2002a, *MNRAS*, **332**, 827

Norberg, P., et al. 2002b, *MNRAS*, **336**, 907

Pen, U., Lu, T., van Waerbeke, L., and Mellier, Y. 2003, *MNRAS*, submitted (astro-ph/0304512)

Postman, M., Lauer, T. R., Szapudi, I., and Oegerle, W. 1998, *ApJ*, **506**, 33

Réfrégier, A., Rhodes, J., and Groth, E. J. 2002, *ApJ*, **572**, L131

Sawicki, M. J., Lin, H., and Yee, H. K. C. 1997, *AJ*, **113**, 1

Somerville, R. S., Lee, K., Ferguson, H. C., Gardner, J. P., Moustakas, L. A., and Giavalisco, M. 2003, *ApJ*, in press (astro-ph/0309071)

Spergel, D. N., et al. 2003, *ApJS*, **148**, 175

Steidel, C. C., Adelberger, K. L., Giavalisco, M., Dickinson, M., and Pettini, M. 1999, *ApJ*, **519**, 1

Steidel, C. C., Adelberger, K. L., Shapley, A. E., Pettini, M., Dickinson, M., and Giavalisco, M. 2003, *ApJ*, **592**, 728

Steidel, C. C., Giavalisco, M., Pettini, M., Dickinson, M., and Adelberger, K. L. 1996, *ApJ*, **462**, L17

Szalay, A. S., Connolly, A. J., and Szokoly, G. P. 1999, *AJ*, **117**, 68

Van Waerbeke, L. and Mellier, Y. 2003, preprint (astro-ph/0305089)

Van Waerbeke, L., Mellier, Y., Pelló, R., Pen, U.-L., McCracken, H. J., and Jain, B. 2002, *A&A*, **393**, 369

Van Waerbeke, L., et al. 2001, *A&A*, **374**, 757

Williams, R. E., et al. 1996, *AJ*, **112**, 1335

Yee, H. K. C. 1998, in *Proceeding of the Xth Rencontres des Blois: Birth of Galaxies* (astro-ph/9809347)

York, D. G., et al. 2000, *AJ*, **120**, 1579

Zehavi, I., et al. 2002, *ApJ*, **571**, 172